Geochemistry Geophysics Geosystems G3
AN ELECTRONIC JOURNAL OF THE EARTH SCIENCES
Published by AGU and the Geochemical Society

Article
Volume 11, Number 1
27 January 2010
Q01Z11, doi:10.1029/2009GC002916
ISSN: 1525-2027

Detection of noninteracting single domain particles using first-order reversal curve diagrams

Ramon Egli, Amy P. Chen, and Michael Winklhofer
Department of Earth and Environmental Sciences, Ludwig-Maximilians University, Theresienstrasse 41, D-80333 Munich, Germany (egli@geophysik.uni-muenchen.de)

Kenneth P. Kodama
Department of Earth and Environmental Sciences, Lehigh University, Bethlehem, Pennsylvania 18015-3188, USA

Chorng-Shern Horng
Institute of Earth Sciences, Academia Sinica, PO Box 1-55, Taipei 115, Taiwan

[1] We present a highly sensitive and accurate method for quantitative detection and characterization of noninteracting or weakly interacting uniaxial single domain particles (UNISD) in rocks and sediments. The method is based on high-resolution measurements of first-order reversal curves (FORCs). UNISD particles have a unique FORC signature that can be used to isolate their contribution among other magnetic components. This signature has a narrow ridge along the H_c axis of the FORC diagram, called the central ridge, which is proportional to the switching field distribution of the particles. Therefore, the central ridge is directly comparable with other magnetic measurements, such as remanent magnetization curves, with the advantage of being fully selective to SD particles, rather than other magnetic components. This selectivity is unmatched by other magnetic unmixing methods, and offers useful applications ranging from characterization of SD particles for paleointensity studies to detecting magnetofossils and ultrafine authigenically precipitated minerals in sediments.

Components: 10,960 words, 12 figures, 3 tables.

Keywords: magnetofossils; first-order reversal curves; single domain particles; magnetic unmixing.

Index Terms: 1505 Geomagnetism and Paleomagnetism: Biogenic magnetic minerals; 1512 Geomagnetism and Paleomagnetism: Environmental magnetism; 1540 Geomagnetism and Paleomagnetism: Rock and mineral magnetism.

Received 21 October 2009; **Revised** 7 November 2009; **Accepted** 11 November 2009; **Published** 27 January 2010.

Egli, R., A. P. Chen, M. Winklhofer, K. P. Kodama, and C.-S. Horng (2010), Detection of noninteracting single domain particles using first-order reversal curve diagrams, *Geochem. Geophys. Geosyst.*, *11*, Q01Z11, doi:10.1029/2009GC002916.

Theme: Magnetism From Atomic to Planetary Scales: Physical Principles and Interdisciplinary Applications in Geoscience
Guest Editors: J. Feinberg, F. Florindo, B. Moskowitz, and A. P. Roberts

1. Introduction

[2] Single domain (SD) magnetic particles have been the subject of intense research in material sciences and in paleomagnetism and environmental magnetism for more than 70 years because of their stability as remanent magnetization carriers. Strictly quantitative theories on recording the Earth's magnetic field in rocks exist only for noninteracting or weakly interacting SD particles [*Shcherbakov and Sycheva*, 1996]. Therefore, rocks and single crystals containing such particles as the predominant magnetic phase are ideal for paleointensity studies [*Tarduno et al.*, 2006]. Ultrafine magnetic particles with grain size distributions typically covering the superparamagnetic (SP) and SD range also form authigenically in sediments and soils where they can be an important source of a stable natural remanent magnetization (NRM), as well as being a paleoenvironmental tracer. Since discovery of biomineralized magnetite in Chiton teeth [*Lowenstam*, 1962], in magnetotactic bacteria [*Bellini*, 1963; *Blakemore*, 1975; *Frankel et al.*, 1979] and by dissimilatory iron reducing bacteria [*Lovley et al.*, 1987], biogenic magnetic minerals have been found in sediments and sedimentary rocks globally. Magnetotactic bacteria are of particular interest because they synthesize chains of SD crystals (magnetosomes) with extremely well-controlled sizes and shapes. Magnetosomes can be preserved over geologically significant times, if they survive diagenesis, in which case they are called magnetofossils [*Kirschvink and Chang*, 1984]. Magnetofossils have been found in a variety of marine and freshwater sediments and sedimentary rocks [e.g., *Petersen et al.*, 1986; *Chang et al.*, 1987; *Snowball*, 1994], where they can contribute >60% to the saturation remanent magnetization [*Egli*, 2004a, 2004b]. Magnetofossils are also of interest in paleoenvironmental studies because they provide information about past geochemical conditions that favored growth of magnetotactic bacteria and/or that controlled the preservation or dissolution of magnetosomes [e.g., *Hesse and Stolz*, 1999].

[3] When magnetosomes are preserved over geological times they become exceptionally stable NRM carriers provided that the chain structure is prevented from collapsing [*Kirschvink*, 1982; *McNeill and Kirschvink*, 1993; *Shcherbakov et al.*, 1997; *Kobayashi et al.*, 2006]. The importance and efficiency of magnetofossils as NRM carriers, along with the physical process they record, are largely unknown. A depositional remanent magnetization model suggests that aggregation of ultrafine magnetic particles during deposition does not lead to formation of chain structures [*Shcherbakov and Sycheva*, 2008]. This implies that isolated chains of magnetite particles in sediments are exclusively of bacterial origin. On the other hand, nonisolated magnetic chain structures occur in silicate-hosted (titano)magnetite inclusions, where the host crystal provides a template for their growth [*Feinberg et al.*, 2006], and in heated Fe-rich carbonates [*Golden et al.*, 2001]. Such structures are, however, magnetically distinct from biologically produced chains.

[4] Precise characterization of SD particles is desirable for many purposes, ranging from selection of suitable rocks for paleointensity determinations to studying biogeochemical iron cycling in sediments. The main obstacle to such characterization is the admixture of other magnetic components, because even the most sophisticated magnetic unmixing methods suffer from limitations that prevent a fully quantitative solution. First-order reversal curve (FORC) diagrams [*Wilde and Girke*, 1959] provide a characterization tool for magnetic fingerprinting, with particular focus on probing magnetostatic interactions [*Pike et al.*, 1999], switching mechanisms [*Pike and Fernandez*, 1999], and domain state and composition [*Roberts et al.*, 2000]. Applications of FORC diagrams in the geosciences range from an aid for the preselection of appropriate samples for paleointensity determinations [e.g., *Wehland et al.*, 2005; *Carvallo et al.*, 2006; *Tarduno et al.*, 2006; *Yamazaki*, 2008], to the characterization of sediments [*Roberts et al.*, 2006; *Rowan and Roberts*, 2006] and magnetosome growth in magnetotactic bacteria [*Pan et al.*, 2005; *Li et al.*, 2009; *Carvallo et al.*, 2009].

[5] An exact FORC model for Stoner-Wohlfarth (SW) particles [*Stoner and Wohlfarth*, 1948] has been elaborated by *Newell* [2005], followed by theoretical analysis of weak magnetostatic interactions in diluted dispersions of such particles [*Egli*, 2006a]. These works provide the basis for understanding the FORC signatures of well dispersed SD particles. One of these signatures, consisting of a narrow ridge concentrated on the H_c axis of a FORC diagram, is expected to be clearly identifiable even in complex mixtures with other magnetic components. This signature has sometimes been recognized in natural samples [e.g., *Roberts et al.*, 2000; *Yamazaki*, 2008; *Abrajevitch and Kodama*, 2009] and cultured magnetotactic bacteria [*Li et al.*, 2009], without further quantitative interpretation, but more often than not it has been overlooked, due to insuffi-

cient measurement resolution or incorrect data processing.

[6] We present a precise FORC method for quantifying noninteracting or weakly interacting uniaxial SD particles, hereafter collectively referred to as UNISD particles. Although FORC measurements are not particularly rapid, they are completely automated by the software that controls the Micromag® vibrating sample magnetometer (VSM) and the alternating gradient magnetometer (AGM). This method can therefore be used to calibrate rapid magnetic characterization methods for analysis of larger numbers of samples. Importantly, we believe our approach provides a uniquely diagnostic method for characterizing UNISD particles, which opens up new opportunities for detecting fossil magnetosome chains in sediments.

2. Magnetic Methods for Magnetofossil Identification

[7] The simplest nondestructive methods for magnetofossil identification are based on two bulk magnetic parameters: the ratio between anhysteretic remanent magnetization (ARM) and isothermal remanent magnetization (IRM) or low field susceptibility χ, and the crossover R_{af} between remanent acquisition and alternating field (AF) demagnetization curves [*Cisowski*, 1981; *Moskowitz et al.*, 1993; *Snowball et al.*, 2002]. ARM ratios are sensitive domain-state indicators, with highest values for SD particles (typically χ_{ARM}/IRM > 1 mm/A and $\chi_{ARM}/\chi > 10$), while crossover values close to 0.5 are characteristic of noninteracting SD particles and magnetosome chains. The disadvantage of these methods is that bulk magnetic parameters do not allow unique interpretation with nonnegligible additional contributions from other magnetic components.

[8] A specific test for the presence of magnetite magnetofossils is based on the distinctive Verwey transition features of linear chains of SD magnetite particles. The ratio δ_{FC}/δ_{ZFC} enables characterization of magnetization losses across the Verwey transition using thermal demagnetization curves of field-cooled (FC) and zero-field-cooled (ZFC) induced remanence, and is systematically higher for magnetosome chains ($\delta_{FC}/\delta_{ZFC} > 2$) than for other magnetite particles of any domain state [*Moskowitz et al.*, 1993; *Carter-Stiglitz et al.*, 2002]. Mixture models can be used to convert δ_{FC}/δ_{ZFC} into a magnetosome fraction [*Moskowitz et al.*, 1993; *Kim et al.*, 2005; *Housen and Moskowitz*, 2006]. Unfortunately, δ_{FC}/δ_{ZFC} is reduced by low-temperature oxidation of magnetite and the chain concentration may be underestimated [*Smirnov and Tarduno*, 2000; *Passier and Dekkers*, 2002].

[9] Precise magnetosome shape and volume constraints mean that magnetofossil chains are characterized by a narrow distribution of switching fields, which is not matched by other known natural magnetic components. This property has been exploited by coercivity analysis [*Egli*, 2003, 2004a] and ferromagnetic resonance (FMR) spectroscopy [*Weiss et al.*, 2004; *Kopp et al.*, 2006]. With coercivity analysis, high-resolution AF demagnetization curves of ARM and IRM are used to calculate the corresponding switching field distributions, which are fitted using appropriate model functions. Each model function is identified with a magnetic component for which $r_a = \chi_{ARM}$/IRM is calculated. In most cases, r_a of magnetofossil components is close to theoretical values for SD magnetite [*Egli and Lowrie*, 2002; *Egli*, 2004a]. This suggests that magnetofossils or magnetofossil chains must be extremely well dispersed in the sediment matrix, given the sensitivity of ARM to magnetostatic interactions [*Egli*, 2006b]. Therefore, magnetofossil-related UNISD signatures are expected to be common in sediments. Coercivity analysis gives strictly quantitative results; however, it is time consuming and becomes unstable with increasing numbers of magnetic components. FMR spectra can be analyzed in a manner similar to magnetization curves, by isolating different anisotropy contributions and fitting spectra with model curves. These methods have limitations when interpreting complex magnetic mixtures, which are overcome with FORC measurements. We propose a suitable FORC measurement protocol for samples containing UNISD particles, and provide a theoretical framework for interpreting the corresponding FORC diagrams.

3. FORC Measurement and Data Processing Protocol

3.1. FORC Diagrams

[10] FORCs are partial hysteresis curves that originate from the same branch of the major loop, which is the descending branch in most measurement protocols. To measure a single FORC, a positive saturation field, H_s, is first applied and it is then decreased to a so-called reversal field, H_r. Starting from H_r, the field is increased in steps of size δH and the in-field magnetization $M(H_r, H)$ is measured

at each field step H. A family of N ascending FORCs consists of a collection of these partial hysteresis curves starting with different H_r values that are offset by δH from one curve to the next. The FORC function,

$$\rho(H_r, H) = -\frac{1}{2}\frac{\partial^2 M(H_r, H)}{\partial H_r \partial H} \quad (1)$$

[*Wilde and Girke*, 1959; *Mayergoyz*, 1986; *Pike et al.*, 1999], is defined on a half plane, called FORC space, that is occupied by the measurement coordinates (H_r, $H \geq H_r$). The transformed coordinates $H_c = (H - H_r)/2$ and $H_u = (H + H_r)/2$ are commonly used for graphical representation. The (H_c, H_u) coordinate system is motivated by the phenomenological Preisach theory, in which H_c and H_u correspond to the coercivity and the bias field, respectively, of elemental rectangular hysteresis loops called hysterons [*Preisach*, 1935]. A limitation of interpreting FORC measurements in terms of the Preisach theory is that hysteresis loops of individual particles generally cannot be approximated by rectangular hysterons [*Pike and Fernandez*, 1999; *Newell*, 2005; *Dumas et al.*, 2007].

[11] High-precision FORC models have been developed for UNISD particles [*Newell*, 2005], and for weak dipolar interactions [*Egli*, 2006a]. The FORC function of UNISD particles can be effectively decomposed into (1) an infinitely sharp ridge $\rho_{cr}(H_c, H_u = 0)$ concentrated along the H_c axis, to which we refer as the central ridge, and (2) a continuous function $\rho_{ur}(H_c, H_u < 0)$ that is antisymmetric about the H_r axis and negative in the lower left-hand domain of FORC space [*Newell*, 2005]. The central ridge corresponds to irreversible magnetization changes (i.e., moment switching of individual particles), while the continuous part represents differences in reversible magnetization changes that depend on H_r (i.e., rotation of magnetic moments in the applied field). The central ridge can be broadened by thermal relaxation effects [*Egli*, 2006a]. Other effects of thermal activations, observed in samples containing viscous particles, include a shift of the central peak to lower coercivities and the onset of a positive contribution near the H_u axis [*Pike et al.*, 2001a].

[12] Magnetostatic interactions convert the central ridge into a function of finite width [*Pike et al.*, 1999]. The case for SD particles homogeneously diluted in a nonmagnetic matrix is well understood and has been modeled analytically [*Egli*, 2006a]. FORC functions of such particles are roughly symmetric about the H_c axis, and have typical teardrop shaped contours [*Pike et al.*, 1999; *Egli*, 2006a]. Strong interactions, on the other hand, are difficult to model because interaction fields depend on the magnetization [*Muxworthy and Williams*, 2005]. A variety of FORC diagrams with oval contours is obtained in this case [*Pike et al.*, 1999]. Dense magnetosome aggregates, such as those originating from chain collapse or magnetic extraction, are characterized by a FORC diagram with oval or teardrop shaped contours that extend well into the $H_u \geq 0$ region by up to 60 mT [*Chen et al.*, 2007]. FORC diagrams of sediments containing SD greigite usually have strong interaction features, often accompanied by a downward shift of the central maximum [*Roberts et al.*, 2000, 2006; *Rowan and Roberts*, 2006; *Florindo et al.*, 2007; *Vasiliev et al.*, 2007]. FORC diagrams of pseudo–single domain (PSD) or multidomain (MD) particles have a large spread along H_u, and are roughly reflection symmetric about the H_c axis [*Roberts et al.*, 2000; *Pike et al.*, 2001b; *Muxworthy and Dunlop*, 2002]. A narrow ridge along the H_c axis has never been observed for such particles, which supports the conclusion that it is a unique feature of SD particles.

[13] The FORC signature of authigenically precipitated ultrafine magnetite or greigite depends on how well these particles are dispersed in the sediment matrix, and is largely unknown. There is some evidence that pedogenic magnetite is not affected by strong magnetostatic interactions and could contribute to a narrow ridge centered along the H_c axis [*Geiss et al.*, 2008].

[14] Fossil magnetosome chains can be expected to occur in isolated form in the sediment matrix, because the magnetotactic bacteria cell body should have prevented the formation of clusters, providing enough distance to make magnetostatic interaction effects negligible, as observed in cultured magnetotactic bacteria samples [*Moskowitz et al.*, 1993]. Isolated chains of mature magnetosomes are magnetically equivalent to UNISD particles because all crystals in a chain switch at the same critical field [*Penninga et al.*, 1995; *Hanzlik et al.*, 2002]. An exception is represented by magnetotactic bacteria containing magnetosome chain bundles [*Hanzlik et al.*, 2002] or magnetosome clusters [e.g., *Faivre and Schüler*, 2008, Figure 1c]. Sediments containing abundant magnetofossils are thus expected to display all FORC signatures of UNISD particles. This is confirmed for the first time in

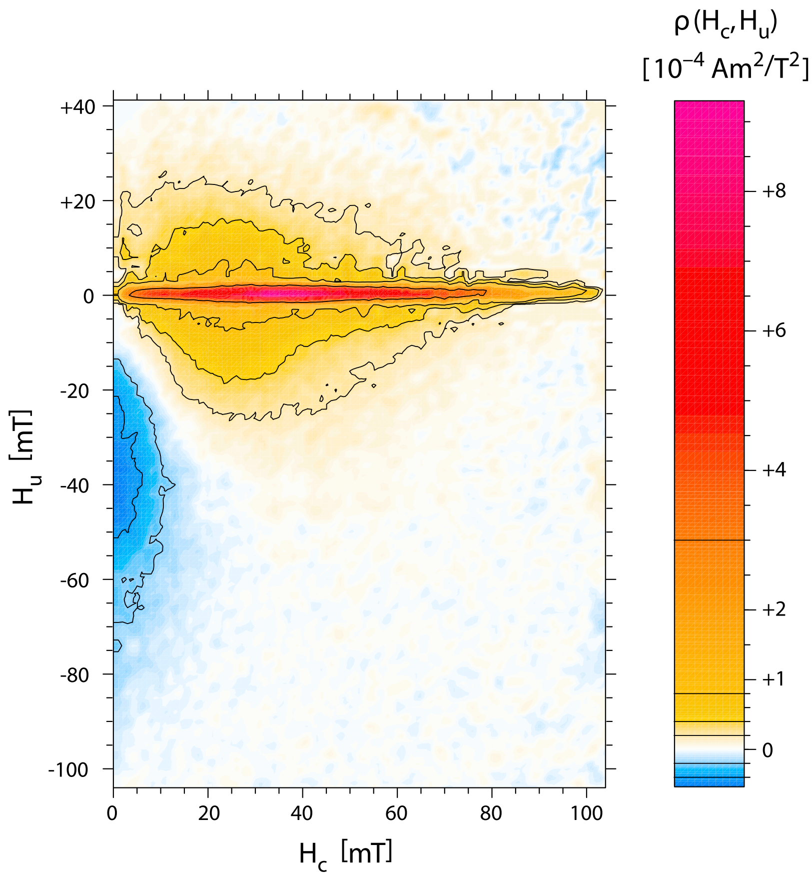

Figure 1. High-resolution FORC diagram for a sediment sample from Lake Ely (Pennsylvania). Note the one order of magnitude difference between the amplitude of the central ridge and the remaining part of the diagram. The color scale is chosen so that zero is white, negative values are blue, and positive values are yellow to red. Contour lines are drawn for values specified in the color scale bar. Measurements are not normalized by mass.

Figure 1 on a sample from Lake Ely (Pennsylvania) [*Kim et al.*, 2005].

3.2. Selecting Suitable FORC Measurement Parameters

[15] Suitable measurement parameters must be chosen to correctly resolve the FORC signatures of UNISD particles. The FORC acquisition procedure is automated by the Micromag® software that controls the VSM or the AGM. At the start of the experiment, the user is prompted to input: the saturating field H_s, the H_u range (given by "Hb1" and "Hb2"), the H_c range (given by "Hc1" and "Hc2"), the averaging time, the field increment δH, the number N of FORC curves to be measured, and other parameters that are not discussed here. Best choice of the measurement parameters depends on the sample. Given the low concentration of magnetic minerals in typical sediments, it is important to select the smallest possible measurement range. Typical averaging times are between 0.2 and 1 s. Increasing the averaging time helps to reduce measurement noise, except for the noise deriving from the electromagnets, but it also increases instrumental drift effects. Therefore, averaging multiple FORC runs is more effective than increasing the averaging time in case of particularly weak samples. Care should be taken to avoid drift artifacts, which are particularly pronounced during the first 20 min of instrument operation and are not completely removable by data processing.

[16] The most critical parameters are the H_c and H_u ranges, which determine the FORC space covered by the measurement, and the field increment δH (Figure 2). If $\hat{H}_c$ is the largest switching field of interest, and if the FORC diagram is expected to extend by $\hat{H}_u$ above the H_c axis, sufficient FORC space coverage with minimum amount of measurements is obtained by choosing Hc1 = 0, Hc2 $\geq \hat{H}_c$, Hb1 = $-\hat{H}_c - \hat{H}_u$, and Hb2 = $\hat{H}_u$. The last two important measurement parameters are the field increment δH and the number N of FORC curves.

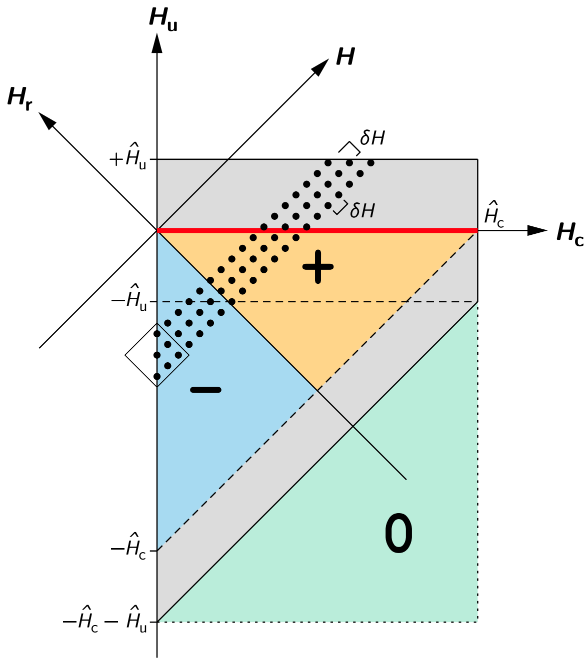

Figure 2. The FORC space in (H_r, H) and (H_c, H_u) coordinates. Dots indicate the measurement points for three consecutive FORCs, spaced by δH. The blue and yellow triangular regions are the positive and negative regions of the FORC function for noninteracting SD particles with switching fields $0 < H_{sw} \leq \hat{H}_c$. The red line along the H_c axis is the central ridge for such particles. In the case of interactions or mixtures with PSD/MD components, the FORC function extends over a larger range indicated by the gray region. The FORC function over the green triangular region is zero. The square centered on the H_u axis contains the $(2SF + 1) \times (2SF + 1)$ array of points (with $SF = 1$ in this example) used to calculate the FORC function corresponding to the middle point of the square. The array is incomplete in this location because the region to the left of the H_u axis does not contain data points.

The Micromag® software automatically calculates either of these two parameters depending on which one the user keeps fixed. The choice of δH dictates the smallest details that can be resolved in FORC space, and is of particular importance for resolving the central ridge. Measurements with resolution $\delta H > 0$ unavoidably widen the central ridge. This effect, which also depends on the smoothing factor SF chosen for data processing, must be maintained within acceptable limits, thereby constraining δH to the values listed in Tables 1 and 2.

3.3. FORC Data Processing

[17] To address the specific processing requirements of FORC diagrams related to UNISD particles, the FORC processing code written in MATLAB® [*Winklhofer and Zimanyi*, 2006] was extended to a new version called "UNIFORC." In UNIFORC, the mixed derivative of equation (1) is calculated either by polynomial fits over squared arrays of $(2SF + 1) \times (2SF + 1)$ measurement points, or directly by finite differences. In the latter case, finite differences are filtered by averaging over the same square arrays (Figure 2). The direct method based on finite differences is less prone to artifacts when dealing with noisy data.

[18] The mixed derivative calculation is particularly critical near the edges of the FORC space (e.g., the H_u axis). Edges are problematic for numerical differentiation methods requiring a rectangular set of data points, which is, by nature, incomplete near $H = H_r$ (Figure 2). *Pike* [2003] suggested extending each FORC into $H < H_r$ (magnetization-extended FORC) by extrapolating a constant magnetization (Figure 3). The ideal magnetization-extended FORC function contains an infinitely sharp ridge, called the reversible ridge, on the H_u axis, which accounts for reversible magnetization processes that are not recorded in FORC space. The finite resolution of real measurements, however, shifts this ridge into FORC space, where it often overshadows low-coercivity FORC contributions (e.g., Figure 4a). This effect is particularly evident in samples where reversible magnetization processes are dominant, which leads to the widespread practice of clipping the region near $H_c = 0$ [e.g., *Roberts et al.*, 2006]. This problem is avoided in UNIFORC by assuming that each FORC is point

Table 1. Optimal Choice of FORC Parameters to Measure the Central Ridge[a]

	SF = 3	SF = 4	SF = 5	SF = 6	SF = 7
H_{c1}, H_{c2} (mT)	0, 110	0, 110	0, 110	0, 110	0, 110
H_{u1}, H_{u2} (mT)	−15, +15	−15, +15	−15, +15	−15, +15	−15, +15
δH (mT)	≤0.83	≤0.63	≤0.50	≤0.42	≤0.36
Estimated measurement time (hours)	≥2.3	≥3.7	≥5.4	≥7.4	≥9.8

[a] Maximum switching field $\hat{H}_{sw}$ = 110 mT and FORC resolution ΔH = 2.5 mT.

Table 2. Optimal Choice of FORC Parameters to Measure the Entire FORC Function[a]

	SF = 3	SF = 4	SF = 5	SF = 6	SF = 7
H_{c1}, H_{c2} (mT)	0, 110	0, 110	0, 110	0, 110	0, 110
H_{u1}, H_{u2} (mT)	−40, +40	−40, +40	−40, +40	−40, +40	−40, +40
δH (mT)	≤0.83	≤0.63	≤0.50	≤0.42	≤0.36
Estimated measurement time (hours)	≥3.4	≥5.5	≥8.3	≥11.3	≥15

[a] Maximum switching field $\hat{H}_{sw}$ = 110 mT and FORC resolution ΔH = 2.5 mT.

symmetric about $H = H_r$. A "slope extended" FORC, defined as

$$M^*(H_r, H) = \begin{cases} 2M(H_r, H_r) - M(H_r, 2H_r - H) & \text{if } H < H_r \\ M(H_r, H) & \text{if } H \geq H_r \end{cases} \quad (2)$$

does not inflect sharply at $H = H_r$, and the reversible ridge is removed from FORC space. The information conveyed by this ridge can be plotted separately [*Winklhofer et al.*, 2008].

3.4. FORC Measurements for Two Sediment Samples

[19] FORC diagrams for two natural samples illustrate our approach. They include a sediment from Lake Ely (Pennsylvania), which is known to contain abundant magnetofossils [*Kim et al.*, 2005], and a marine greigite-bearing sediment recovered off the southwestern Taiwan coast (core ORI-758 GH3, 22°16.8N, 119°48.6E, see *Horng and Chen* [2006] for description of cores from the same site). The three FORC diagrams shown in Figure 4 were obtained from the same Lake Ely sample, and, with the exception of the H_u range, H_c range, and δH, all other measurement parameters were the same. The main feature of the FORC diagrams is a distribution centered on the H_c axis whose width along H_u is different in each case. This difference does not come from the choice of the H_u and H_c ranges or from data processing, which are identical in Figures 4b and 4c.

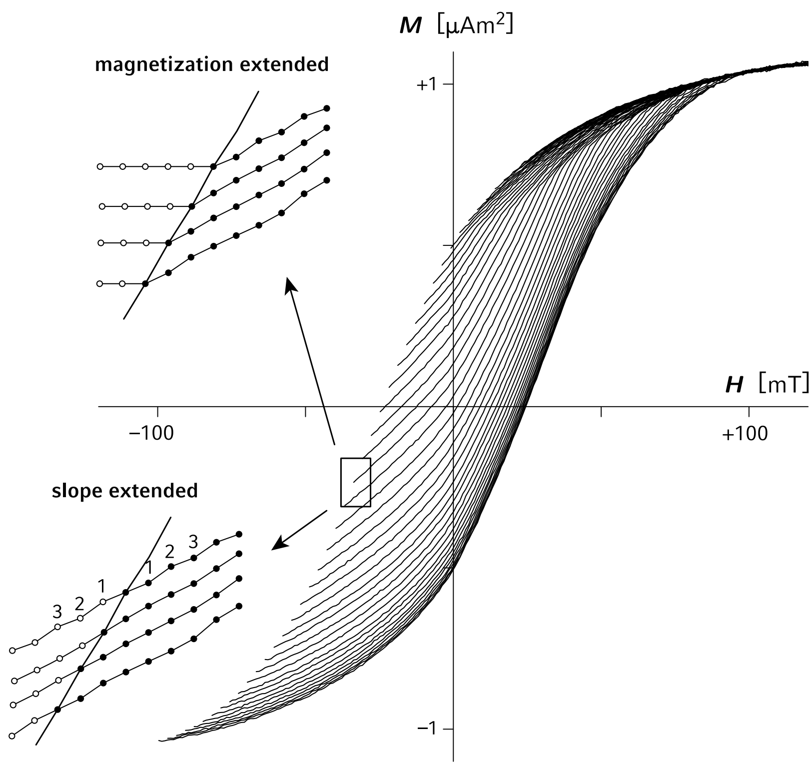

Figure 3. Set of 197 FORCs for the studied Lake Ely sample. Every third FORC after subtraction of the paramagnetic mineral contribution is shown for clarity. The two insets on the left are magnifications of the region marked by the rectangle, where all measured FORCs (solid circles) are plotted for the magnetization extended and slope extended cases (open circles). In the slope extended case, numbers indicate how three points in the FORC space are reflected left from $H = H_r$.

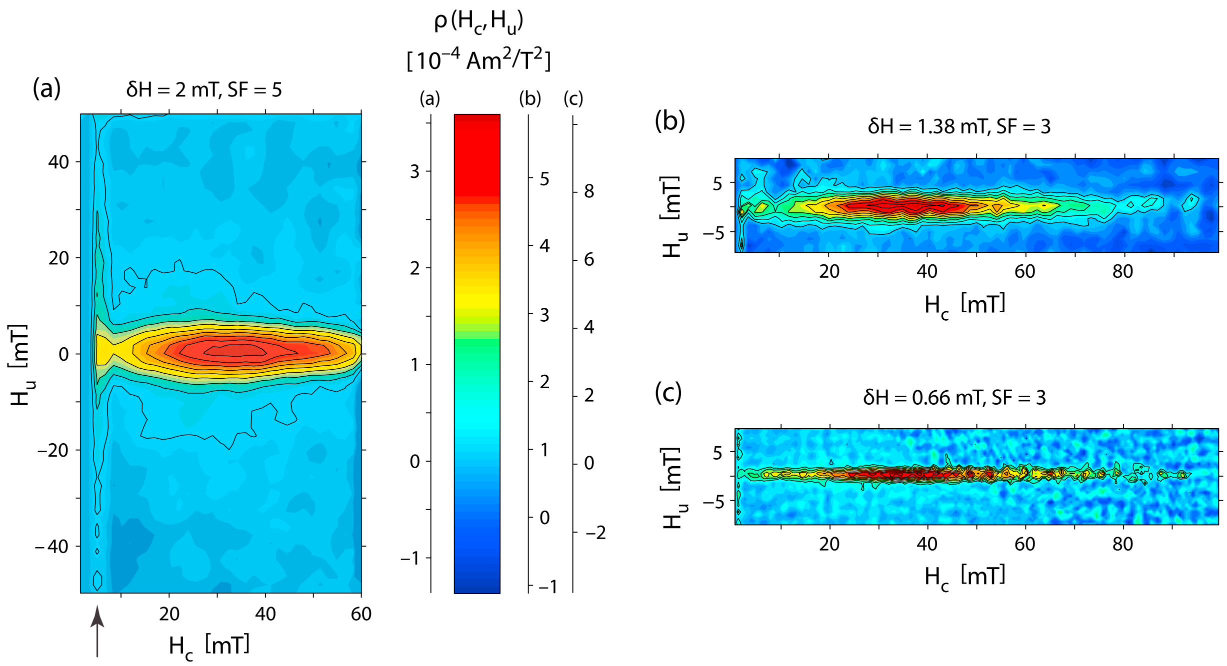

Figure 4. FORC diagrams measured on the Lake Ely sediment sample using different parameters. (a) $\delta H = 2$ mT, $SF = 5$, and $\Delta H = 10$ mT; (b) $\delta H = 1.38$ mT, $SF = 3$, and $\Delta H = 4.1$ mT; and (c) $\delta H = 0.66$ mT, $SF = 3$, and $\Delta H = 2$ mT. Measurements were processed with the magnetization extended algorithm, which adds the reversible ridge. This ridge, which is ideally of infinitesimal width and located at $H_c = 0$, is broadened and shifted to $H_c \approx 5$ mT (arrow) in the example in Figure 4a with lowest resolution. Note that each plot has a different scale bar.

This demonstrates the role of δH in resolving the central ridge. FORC measurements in Figure 4 were processed using the magnetization extended method discussed in section 3.3, in which the reversible ridge encroaches into the low-H_c region of FORC space: this effect is particularly evident with low measurement resolution (Figure 4a). FORC diagrams shown in Figure 5 were obtained from the Taiwan greigite-bearing sample. In this case, unlike the Lake Ely sample, a more than fivefold difference in δH has negligible effect on the shape of the FORC diagram, except for the amplitude of measurement noise.

[20] Why should the FORC function width along H_u be controlled by δH for the Lake Ely sample but not for the Taiwan greigite-bearing sample? This question can be answered by inspecting a plot of the full width at half maximum (FWHM) of the H_u profile taken at the FORC distribution peak, versus $\Delta H = \delta H \times (SF + 1/2)$ (Figure 6). FWHM for the Lake Ely sample is proportional to ΔH over the entire range of values and converges to zero as $\Delta H \to 0$. This indicates that the true FWHM along H_u is zero or almost zero for UNISD particles. On the other hand, FWHM for the Taiwan greigite-bearing sample converges to 19.5 mT as $\Delta H \to 0$, which is the intrinsic width of the FORC function. It is evident from the Lake Ely example that ΔH is the effective resolution of the FORC diagram, which corresponds to the size of the smallest detail that can be resolved with the user-chosen δH and *SF*. Note that ΔH does not depend on the density of the final grid of (H_c, H_u) coordinates used to represent the FORC function, provided that this is not coarser than the original measurement field increments.

[21] Insufficient measurement resolution not only leads to overlooking the UNISD central ridge, but also to incorrect interpretation. For example, the FORC diagram in Figure 4a could be interpreted as a signature of weakly interacting SD particles. While *SF* optimization has been discussed [*Heslop and Muxworthy*, 2005; *Harrison and Feinberg*, 2008], the importance of δH has not previously been emphasized. The ideal case of $\Delta H = 0$ is not measurable, due to a lower limit for δH imposed by the finite field control precision ($\approx 10\ \mu$T $\pm$ 0.1% of $\hat{H}_c$ for the Princeton Measurement Corporation VSM or AGM). A minimum resolution of 2.5 mT is necessary for correct characterization of the central ridge, as discussed in section 4.6. *SF* values for sedimentary samples usually range from 3 to 7, therefore δH should not exceed 0.3–0.8 mT (Tables 1 and 2).

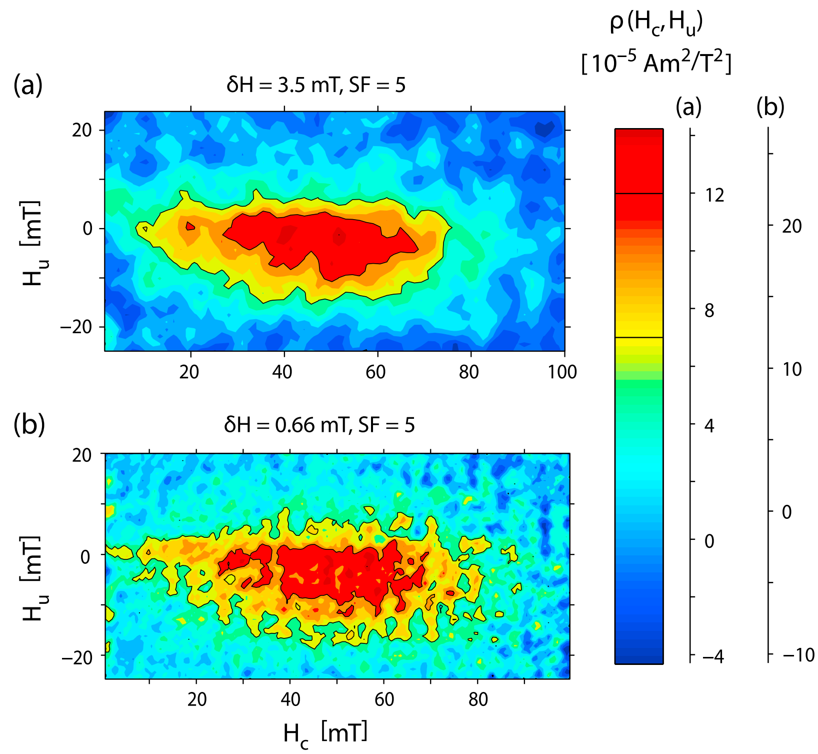

Figure 5. FORC diagrams measured on the Taiwan greigite sample using (a) δH = 3.5 mT, SF = 5, and ΔH = 17.7 mT and (b) δH = 0.66 mT, SF = 5, and ΔH = 3.3 mT. The FORC function is almost identical in the two cases, except for the higher noise level in Figure 5b. Note that each plot has a different scale bar.

[22] After identifying a central ridge in the Lake Ely sample, we performed high-resolution measurements to obtain full coverage of the FORC space (Figure 1). Although Figure 1 is a mosaic of measurements that focus on different domains of the FORC space (for reasons that became obsolete, see the auxiliary material), the same result can be obtained using the measurement parameters listed in Table 2.[1] The sample is magnetically weak; therefore, four identical runs were averaged to improve the signal-to-noise ratio. Individual FORC data sets were preprocessed using UNIFORC and merged into a single diagram. All features of the FORC model calculated by *Newell* [2005] are clearly distinguishable in Figure 1: a central ridge on the H_c axis and a continuous function over $H_u < 0$ that is negative in the lower left-hand part of the diagram. Positive values of the FORC function above the H_c axis reflect magnetic contributions in addition to UNISD particles. The teardrop shaped contours are a typical feature of weakly to moderately interacting SD particles [*Pike et al.*, 1999; *Egli*, 2006a]. Nevertheless, an unquantifiable contribution of larger lithogenic particles cannot be excluded. Contributions from these non-UNISD particles suppress the perfect symmetry of the $H_u < 0$ region about the H_r axis (Figure 1). This can be seen by following the departure of the white region between positive and negative contributions from the $H_u = -H_c$ diagonal. We model the FORC diagram of Figure 1 as the sum of three distinct contributions: (1) a central ridge ρ_{cr} on the H_c axis, produced by irreversible processes associated with UNISD particles; (2) a contribution ρ_{ur} from reversible processes in the same particles, which is antisymmetric about the H_r axis and zero for $H_u > 0$; and (3) a contribution ρ_{other} from other magnetic components, which is roughly symmetric about the H_c axis. Interpretation of these contributions is discussed below.

[1]Auxiliary materials are available in the HTML. doi:10.1029/2009GC002916.

4. Analysis of a FORC Diagram Dominated by SD Particles

[23] The general model described in this section for the FORC distribution of UNISD particles enables establishment of a precise link to other magnetic measurements. This is useful for obtaining the switching field distribution and the saturation remanence of UNISD or weakly interacting SD par-

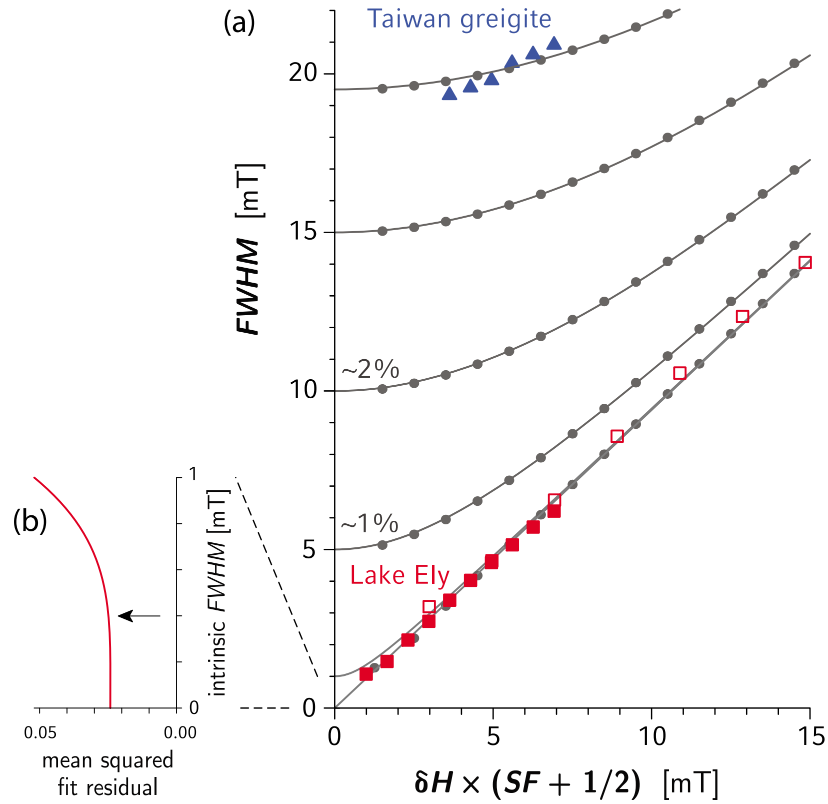

Figure 6. (a) Dependence of the FWHM measured on a vertical profile through the maximum of the FORC function for the Lake Ely sample and the Taiwan greigite sample, as a function of the measurement resolution $\Delta H = \delta H \times (SF + 1/2)$. The intrinsic FWHM is obtained for $\Delta H = 0$. The Lake Ely sample was measured with $\delta H = 0.66$ mT (filled squares). Data for this sample refer to the central ridge only, which has been isolated from other FORC contributions as described in section 4.6. Measurements with $\delta H = 2$ mT (open squares) were obtained by selecting every third H_r and H value from the real measurements. Grey dots are synthetic simulations of central ridges with intrinsic FWHM values of 0, 5, 10, 15, and 19.5 mT, which were processed in the same way as the real FORC diagrams. Grey lines are trends predicted by equation (19). Central ridges with intrinsic FWHM of 5 and 10 mT correspond to homogenous dispersions of SD magnetite particles with a volume concentration of ∼1% and ∼2%, respectively. Data for Lake Ely have been fitted with equation (19) and various values of the intrinsic FWHM between 0 and 1 mT (only 0 and 1 mT are shown). (b) The mean squared fit residual is minimized for intrinsic FWHM values <0.4 mT (arrow).

ticles, even in samples with mixed magnetic components. Application of this theory for identifying SD minerals, and for discriminating among magnetofossils and authigenically precipitated ultrafine magnetic particles, is thoroughly discussed in a companion paper (R. Egli et al., Magnetic characterization of magnetofossils and ultrafine magnetic particles of diagenetic origin, manuscript in preparation, 2010). Proofs of all equations are provided in the auxiliary material.

4.1. FORC Function for Strictly Noninteracting, Uniaxial SD Particles

[24] The FORC function for UNISD particles calculated by *Newell* [2005] using the hysteresis model of *Stoner and Wohlfarth* [1948] can be generalized for uniaxial SD particles requiring more complex models (e.g., including thermal activation effects, or fanning reversal modes for linear particle chains). We consider a sample containing a large number of UNISD particles characterized by a switching field distribution $f(H_{sw})$, where $M_s f(H_{sw})dH_{sw}$ is the contribution of all particles with switching field between H_{sw} and $H_{sw} + dH_{sw}$ to the sample's saturation magnetization M_s. Because $f(H_{sw}) > 0$ and its integral over all switching fields is equal to 1, we can formally consider the switching field distribution as a probability density function (PDF). The hysteresis loop for all particles with the same switching field, normalized by $M_s dH_{sw}$, is composed of an upper and a lower branch, $m_+(H; H_{sw})$ and $m_-(H; H_{sw})$, with discontinuities of amplitude $s(H_{sw})$ at $H =$

$-H_{sw}$ and $H = +H_{sw}$, respectively. Because of inversion symmetry, the two branches can be expressed by the same function $m = m_+$, with $m_-(H) = -m_+(-H)$. Unlike remanent magnetization measurements, where the change in remanence produced by switching is proportional to the particle moment, in-field magnetization jumps depend in detail on the switching mechanism. Magnetization jumps can be negative, acting against the applied field, as for the case of SW particles whose easy axis is almost at right angles to the applied field [*Newell*, 2005, Figure 4].

[25] The FORC function of the particle assemblage described above is given by $\rho = \rho_{cr} + \rho_{ur}$, with the central ridge:

$$\rho_{cr}(H_c, H_u) = \frac{M_s}{2} f(H_c)\, s(H_c)\, \delta(2H_u), \tag{3}$$

where δ is the Dirac delta function. The reversible contribution is given by:

$$\rho_{ur}(H_r, H) = M_s f(-H_r) \frac{m'(-H;-H_r) - m'(H;-H_r)}{2}\, \theta(-H - H_r), \tag{4}$$

where θ is the Heaviside unit step function and m' is the derivative of m with respect to H. The contribution to the FORC function of all particles with switching field H_{sw} is concentrated on a diagonal line connecting the FORC coordinates ($H_c = 0$, $H_u = -H_{sw}$) on the H_u axis with ($H_c = H_{sw}$, $H_u = 0$) on the H_c axis (e.g., a line of points in Figure 2). The continuous part of the FORC diagram along this diagonal is the antisymmetric function $\rho_{ur}(-H_{sw}, H)$ of H with $-H_{sw} < H < +H_{sw}$. In the SW model of *Newell* [2005], ρ_{ur} diverges at both ends of the diagonal (i.e., $H = \pm H_{sw}$), which reflects the fact that $m'(H;\, H_{sw})$ becomes infinite as the discontinuity at $-H_{sw}$ is approached on the upper branch of the loop. This is not the case for real SD particles because switching is assisted by thermal activations and occurs where the slope of $m(H;\, H_{sw})$ is finite.

4.2. Interpretation of the FORC Function in Terms of a Switching Field Distribution

[26] The central ridge in equation (3) is proportional to both the switching field distribution $f(H_c)$ and the magnetization jump amplitude $s(H_c)$. The proportionality to $f(H_c)$ is of interest because it allows interpretation of the central ridge in real FORC measurements (e.g., Figure 1) as the switching field distribution of UNISD particles, while advantageously excluding contributions from non-SD or interacting particles. Coercivity analysis can then be used to identify different magnetic components, as is done with switching field distributions obtained from remanent magnetization curves [e.g., *Egli*, 2003, 2004a]. The important difference between FORC-based and other coercivity analyses is based on the ability to discriminate UNISD particles.

[27] The approach discussed above is possible only if we can show that $s(H_c)$ in equation (3) can be considered a constant. This is not obvious, because both H_{sw} and s are functions of the angle φ between the easy axis and the applied field direction; however, s is practically independent of H_c for typical switching field distributions in natural samples. A switching field distribution is the product of two intrinsic properties: (1) the distribution of easy axis orientations and (2) the distribution of particle anisotropies, expressed by their microcoercivity H_K, which is related to a distribution of particle elongations. Accordingly, the switching field of one particle is written as $H_{sw} = H_K h_{sw}(\varphi)$, where $h_{sw}(\varphi)$ is a function that accounts for the dependence of H_{sw} on the easy axis orientation. For SW particles, $h_{sw}(\varphi)$ is between 0.5 and 1, with most particles having h_{sw} values close to 0.5 if the easy axes are randomly oriented. Given the limited range of h_{sw}, the switching field distribution of natural particle assemblages is largely controlled by the microcoercivity distribution, which we express by a PDF $K(H_K)$ that is defined in the same way as $f(H_{sw})$.

[28] Below, we derive a generic expression for the FORC function of UNISD particle assemblages with microcoercivity distribution $K(H_K)$ and a distribution $p(\varphi)$ of easy axis orientations. Our only limiting assumption is that the shape of the hysteresis loop of individual particles is independent of H_K, as in the SW model. A normalized function $\mu(h;\, \varphi)$ of the applied field $h = H/H_K$ describes the upper branch of the "elemental" hysteresis loop of any particle with easy axis orientation φ. The function is normalized to yield $\mu \to \pm 1$ for $h \to \pm\infty$ (Figure 7a). The assumption that μ describes all elemental hysteresis loops will hold reasonably well for particles from the same magnetic component (e.g., ultrafine magnetite or magnetosome chains), which are expected to switch by the same mechanism (e.g., coherent rotation). We now consider a generic additive property $G(\varphi)$ of the normalized hysteresis loop μ, such as saturation remanence $\mu(0;\, \varphi) = \mu_r(\varphi)$, or amplitude $S(\varphi)$ of the

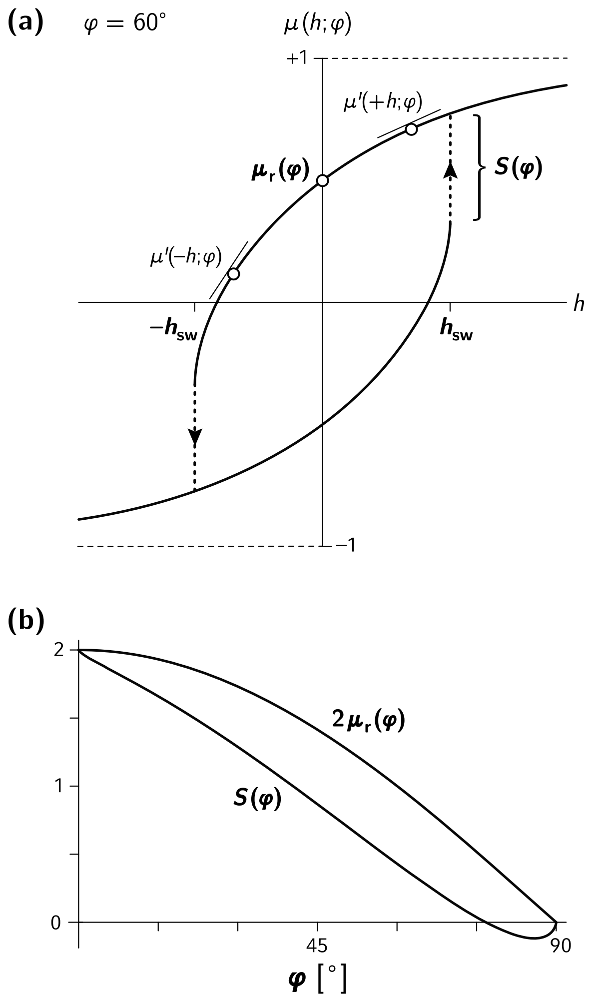

Figure 7. (a) The normalized hysteresis loop $\mu(h;\,\varphi)$ for a uniaxial SD particle (here a SW particle with its easy axis at an angle of 60° to the applied field direction), with two magnetization jumps of amplitude $S(\varphi)$ at $\pm h_{sw}$ (dashed lines) and remanence $\mu_r(\varphi)$. The difference between loop slopes μ' at $\pm h$ determines the reversible component of the FORC function. (b) The magnetization jump amplitude $S(\varphi)$ and the remanence $\mu_r(\varphi)$ of SW particles, as a function of the angle φ between the easy axis and the applied field (solid line). Notice the negative values of $S(\varphi)$ when $\varphi > 76.7°$.

magnetization jump at $h = -h_{sw}$ (Figure 7a). We denote with $g(H_{sw})$ the total contribution of $G(\varphi)$ corresponding to all particles with the same switching field H_{sw}. In all cases, $g(H_{sw})$ is given by:

$$g(H_{sw}) = \int_{\Omega} K\left(\frac{H_{sw}}{h_{sw}(\varphi)}\right) \frac{G(\varphi)}{h_{sw}(\varphi)}\, p(\varphi)\,\mathrm{d}\varphi, \qquad (5)$$

where Ω is the range of φ. Randomly oriented uniaxial particles are characterized by $p(\varphi) = \sin\varphi$ with $0 \le \varphi \le \pi/2$, where $h_{sw}(\varphi)$ for SW particles is given by *Stoner and Wohlfarth* [1948]. The function $G(\varphi)$ is plotted in Figure 7b for examples of saturation remanence and amplitude of the magnetization jumps, using the SW model.

[29] If $K(H_K)$ is a sufficiently wide distribution, $g(H_{sw})$ is proportional to the switching field distribution $f(H_{sw})$, and equation (5) simplifies to:

$$g(H_{sw}) \approx \frac{\overline{G}}{\overline{h}_{sw}} K\left(\frac{H_{sw}}{\overline{h}_{sw}}\right), \qquad (6)$$

where

$$\overline{G} = \int_{\Omega} G(\varphi)\, p(\varphi)\,\mathrm{d}\varphi \qquad (7)$$

is the expected value of $G(\varphi)$, and

$$\overline{h}_{sw} = \frac{1}{\overline{G}} \exp\left[\int_{\Omega} G(\varphi)\, p(\varphi)\, \ln h_{sw}(\varphi)\,\mathrm{d}\varphi\right] \qquad (8)$$

is the logarithmically weighted average of h_{sw} over all easy axis orientations. Equation (6) establishes a direct link between the microcoercivity distribution and any additive magnetic parameter $g(H_{sw})$. The importance of this link becomes clear if we evaluate equation (6) for SW particles, and three important cases of $G(\varphi)$. The first case is $G = 1$, which gives the switching field distribution:

$$f(H_{sw}) \approx \frac{1}{\overline{h}_{sw}} K\left(\frac{H_{sw}}{\overline{h}_{sw}}\right), \qquad (9)$$

with $\overline{h}_{sw} \approx 0.5829$. The second case is the saturation remanence $G = \mu_r$, which gives the derivative of a remanent magnetization curve:

$$M_r'(H_{sw}) \approx \frac{M_s}{2\overline{h}_{sw}} K\left(\frac{H_{sw}}{\overline{h}_{sw}}\right) \approx \frac{M_s}{2} f(H_{sw}), \qquad (10)$$

with $\overline{h}_{sw} \approx 0.5463$. The third case is the amplitude $G = S$ of the magnetization jumps of the hysteresis loops, which gives the central ridge:

$$\rho_{cr}(H_c, H_u) \approx \frac{M_s}{2} \frac{\overline{S}}{\overline{h}_{sw}} K\left(\frac{H_c}{\overline{h}_{sw}}\right) \delta(2H_u) \approx \frac{M_s}{2} \overline{S} f(H_c)\, \delta(2H_u), \qquad (11)$$

with $\overline{h}_{sw} \approx 0.5348$ and $\overline{S} \approx 0.5438$. The values of $\overline{h}_{sw}$ are nearly identical in the three cases: therefore, M_r' and ρ_{cr} are both proportional to $f(H_{sw})$. Equations (9)–(11) are strictly valid only for UNISD particles: this condition is always fulfilled for the central ridge (equation (11)) because it automatically excludes contributions from other particles, but not for remanence measurements (equation (10)), which respond to all particles that hold a remanent magnetization.

[30] The assumption of a "sufficiently wide" microcoercivity distribution can be tested by comparing equations (9)–(11) with the exact solution of equation (5) for different choices of $K(H_K)$. Since $f(H_{sw})$ is typically approximated by a logarithmic Gaussian function [*Robertson and France*, 1994], its width is best expressed by the standard deviation σ of $\log_{10}H_{sw}$. The maximum difference between the exact and approximated solution is 5% for $\sigma = 0.1$, which is the smallest width of a natural component [*Egli*, 2004a]. Therefore, equations (9)–(11) are valid for any natural UNISD particle assemblage.

[31] A similar approach can be used to calculate the reversible component of the FORC function. Using the same assumptions, namely that the shape of the hysteresis loop of individual particles is independent of H_K, and that $K(H_K)$ is sufficiently wide, we obtain:

$$\rho_{ur}(H_r, H) \approx \frac{M_s}{2} f(-H_r) \frac{R(-H/H_r)}{-H_r}, \tag{12}$$

with

$$R(x) = \int_\Omega [\mu'(-xh_{sw}(\varphi);\varphi) - \mu'(xh_{sw}(\varphi);\varphi)]h_{sw}(\varphi)\,p(\varphi)\,\mathrm{d}\varphi \tag{13}$$

being an odd function of $-1 < x < +1$, and μ' the derivative of $\mu(h)$. This means that profiles of ρ_{ur} along diagonals of the FORC space can be expressed by a function R whose argument is scaled to match the length of the diagonal, while the amplitude is modulated by $f(-H_r)$. An example for randomly oriented SW particles is shown in Figure 8. The shape of $R(x)$ depends on the model used to describe the switching mechanism. It is proportional to the difference between the slope of $\mu(h;\varphi)$ evaluated at $+xh_{sw}$ and $-xh_{sw}$ (Figure 7a). The FORC diagram of UNISD particles is completely determined by two functions that reflect the intrinsic properties of the particle assemblage: (1) the switching field distribution $f(H_{sw})$, which is a scaled version of the microcoercivity distribution, and (2) a function R that depends on the switching mechanism.

4.3. Irreversible and Reversible Total FORC Contributions

[32] The total contributions of ρ_{cr} and ρ_{ur} to the FORC function convey important information about the switching mechanism of UNISD particles. We define these contributions as integrals of ρ_{cr} and ρ_{ur} over the FORC space, which have the same unit as the measured FORC curves. Integration in (H_r, H) coordinates over any region of the FORC space yields a result that is twice that obtained in (H_c, H_u) coordinates. We choose (H_r, H) as the reference coordinate system, and define I_{cr} as the integral of the central ridge, and I_{ur} as the integral of ρ_{ur} over the FORC region where it is >0 (i.e., above the H_r axis, see Figure 8b). This choice of I_{ur} is necessary, because the integral of ρ_{ur} over the entire FORC space is zero for symmetry reasons. The two integrals give the following exact result for any system of UNISD particles with any distribution of microcoercivities and any easy axis orientation:

$$\begin{cases} I_{cr} = \dfrac{M_s}{2}\overline{S} \\ I_{ur} = M_{rs} - I_{cr} \end{cases}, \tag{14}$$

where $\overline{S}$ is defined by equation (7) with $G = S$, and M_{rs} is the saturation remanence. For example, SW particles with easy axes parallel to the applied field (i.e., the rectangular hysterons of the Preisach model), have $\overline{S} = S(0) = 2$ and $M_{rs} = 1$. Accordingly, $I_{cr} = M_s$ and $I_{ur} = 0$. Uniaxial particles with randomly oriented easy axes are characterized by $M_{rs} = 0.5$ and $I_{ur} = M_s(1 - \overline{S})/2$, with the ratio

$$\frac{I_{ur}}{I_{cr}} = 1 - \frac{1}{\overline{S}} \tag{15}$$

being a pure function of $\overline{S}$. Equation (15) can be used to compare $\overline{S}$ predicted by hysteresis models (e.g., $\overline{S} \approx 0.5438$ for randomly oriented SW particles) with an empirical estimate $\overline{S}$ obtained from FORC measurements.

4.4. Central Ridge Widening by Magnetostatic Interactions

[33] The distance between SD particles in a sample is finite; therefore magnetostatic interactions are expected to convert the central ridge into a function of finite width. If the effective volume concentration (or packing fraction) p is $\ll 2.7\ \mu_0 H_K/\mu_s$, with H_K and μ_s being the microcoercivity and the

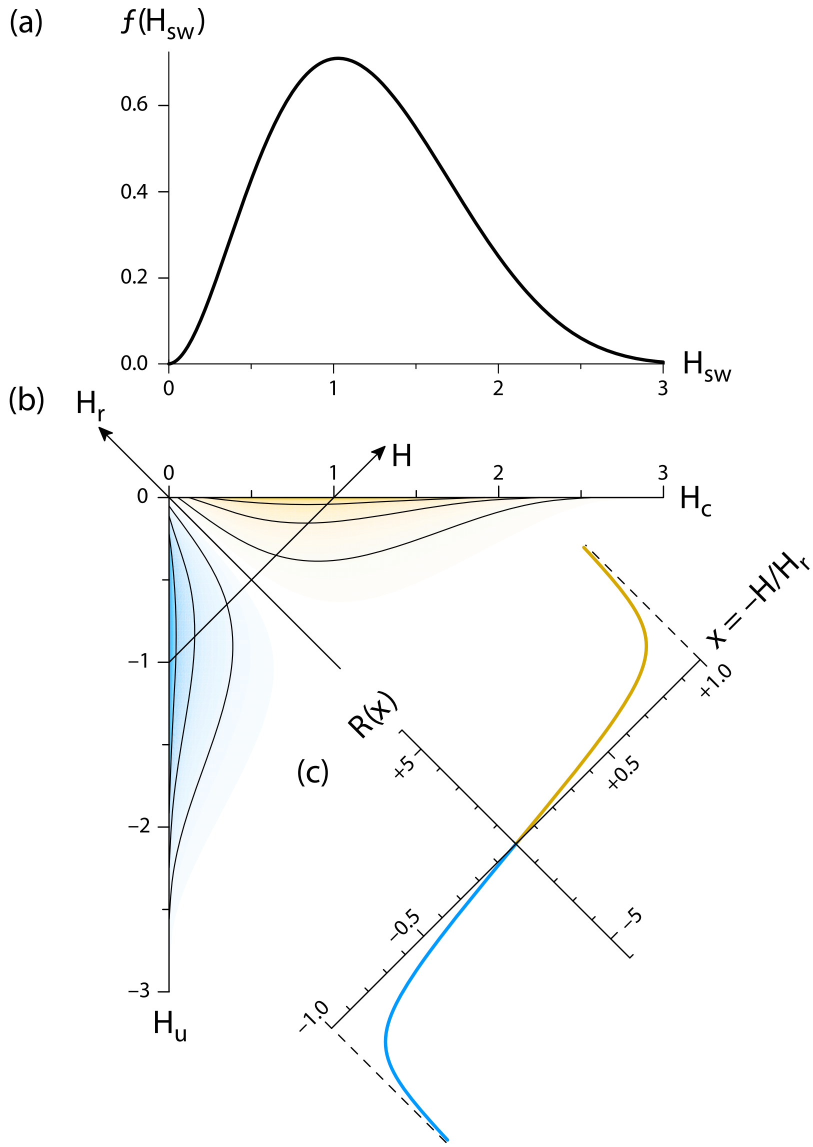

Figure 8. (a) An example of a switching field distribution $f(H_{sw})$ for arbitrary values of H_{sw} and (b) the corresponding reversible component ρ_{ur} of the FORC function. (c) Every profile of ρ_{ur} along the H axis is a rescaled version of the function $R(x)$ defined in equation (13).

spontaneous magnetization of the particles, respectively, we have:

$$\rho_{cr}(H_c, H_u) = \frac{M_s}{2}\,\overline{S} f(H_c)\,\frac{1}{F(H_c)}\,W\!\left(\frac{H_u}{F(H_c)}\right), \text{ and}$$
$$F(H_c) = \int_0^{H_c} f(h)\,\mathrm{d}h, \tag{16}$$

where the interaction field distribution $W(.)$ is the PDF of the interaction field component parallel to the measurement direction [*Egli*, 2006a]. For magnetite particles with $p \leq 2\%$, W in equation (16) is approximated by the Lorentzian function:

$$W(H_u) = \frac{1}{\pi\alpha}\frac{1}{1 + (H_u/\alpha)^2}, \tag{17}$$

where $2\alpha \approx 0.722\ p\mu_s$ is the FWHM of W [*Egli*, 2006a]. For example, the central ridge of a sample containing 1% homogeneously dispersed SD magnetite particles would have FWHM of $\sim$4.3 mT, which is slightly below the measurement resolution if the FORC diagram was measured with 1 mT field steps and SF = 5.

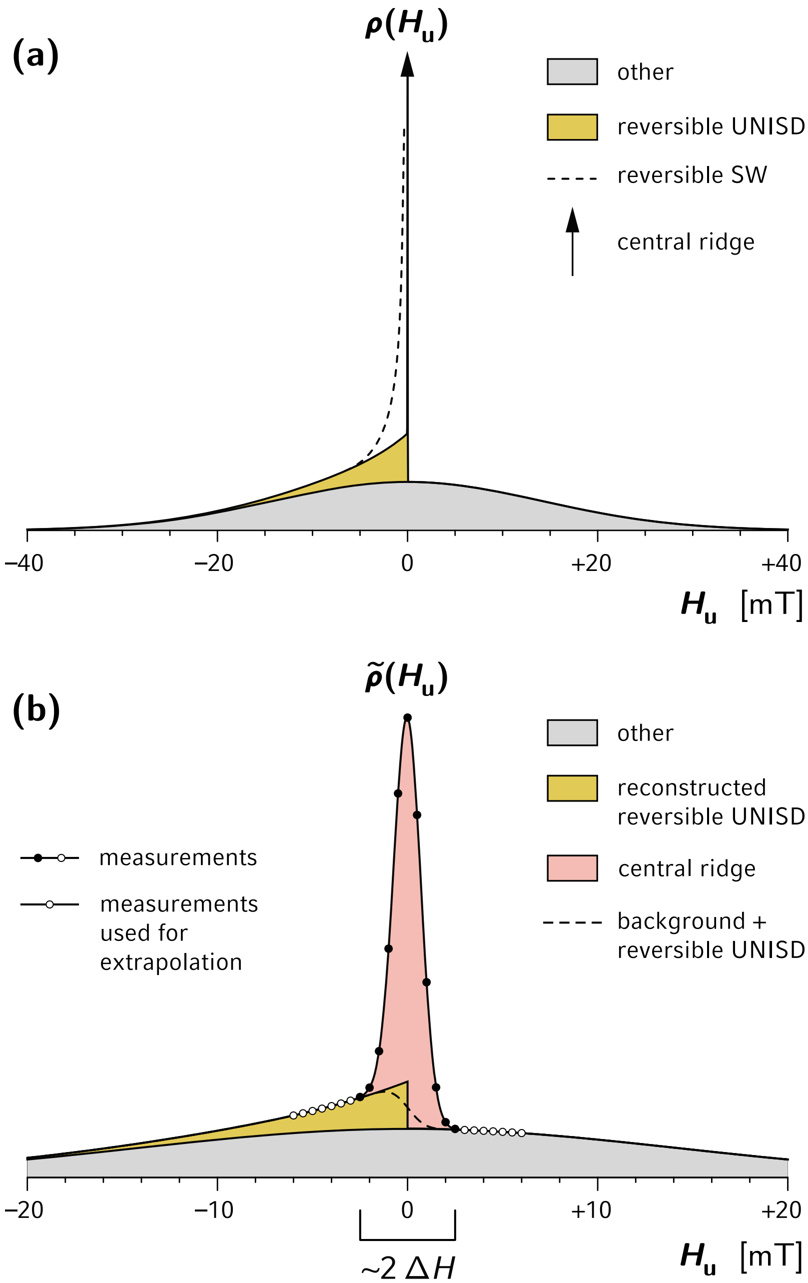

Figure 9. (a) Vertical cross section through an idealized FORC function with infinite resolution. The following contributions are highlighted: the infinitely narrow and infinitely high central ridge produced by UNISD particles (arrow), a continuous background (gray) produced by interacting SD or PSD/MD particles, and the reversible (yellow) contribution of UNISD particles, which is zero for $H_u > 0$. The SW model predicts the reversible contribution to diverge at $H_u = 0$ (dashed line); however, thermal fluctuations have a regularizing effect. (b) The same vertical cross section as in Figure 9a for a more realistic case of FORC measurements with finite resolution. The central ridge is converted to a Gaussian-like function (pink) that extends over $|H_u| < \Delta H$, where ΔH is the resolution of the FORC function. The sum of the background and the UNISD contribution within $|H_u| < \Delta H$ (dashed line) can be reconstructed by extrapolating measurements located just outside this range (open circles). The pink area corresponds to $\mu_{cr}(H_c)$.

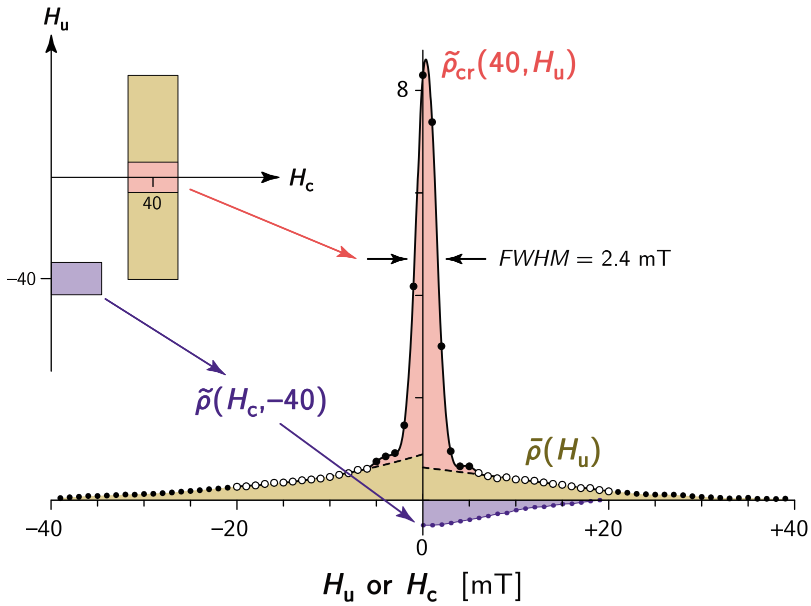

Figure 10. A vertical cross section of the FORC diagram shown in Figure 1, averaged over $30 \le H_c \le 50$ mT (vertical rectangle in the inset). The region occupied by the central ridge, between $H_u = \pm 6$ mT, is clearly recognizable. The next 15 measurement points on each side of this region (open circles) were used to extrapolate the "ridge-free" profile below the central ridge, using two second-order polynomials (dashed lines). The discontinuity at $H_u = 0$ is expected from the reversible component of UNISD particles. A horizontal profile of the negative domain of the FORC diagram (blue), averaged over $-45 \le H_u \le -35$ mT (horizontal rectangle in the inset), is shown for comparison.

4.5. Central Ridge Widening by Data Processing

[34] Measurements and data processing with a combined resolution ΔH convert ρ_{cr} into a smoothed function $\tilde{\rho}_{cr}$ characterized by a larger FWHM. For example, the numerical FORC calculation procedure originally proposed by *Pike et al.* [1999], which is based on piecewise polynomial fits over square regions containing an array of regularly spaced measurement coordinates (H_r, H), is formally equivalent to convolution with a kernel function [*Heslop and Muxworthy*, 2005]. The kernel function works as a derivative operator and as a low-pass filter that reduces measurement errors. The latter operation is conveniently modeled by the convolution of ρ_{cr} with a weighting window $Q(x, y)$:

$$\tilde{\rho}_{cr}(H_r, H) = \int_{-\infty}^{+\infty} dx \int_{-\infty}^{H-H_r} \rho_{cr}(H_r - x, H - y)\, Q(x, y)\, dy, \tag{18}$$

where $Q(x, y)$ depends on the algorithm used for FORC calculation. The simplest example is a moving average window, given by $Q(x, y) = 1/(2\Delta H)^2$ for $|x|$, $|y| \le \Delta H$, and otherwise $Q = 0$. Other choices of $Q(x, y)$ are possible; for example, $Q(r) = (1 - r^3)^{-3}$ is used by the FORCinel algorithm [*Harrison and Feinberg*, 2008], where r is proportional to the Euclidean distance between coordinates. If σ_i is the intrinsic FWHM of ρ_{cr}, and σ_Q is the FWHM of the weighting window, the processed central ridge has a width given by:

$$\mathrm{FWHM} = \sqrt{\sigma_i^2 + \sigma_Q^2/2}. \tag{19}$$

It can be shown by numerical simulation that $\sigma_Q \approx 0.665\ \delta H(2SF + 1)$ for the polynomial fitting procedure of *Pike et al.* [1999] (see auxiliary material and Figure 6). Equation (19) predicts a direct proportionality between FWHM and σ_Q if the central ridge intrinsic width is $\ll \sigma_Q$, as is the case for the Lake Ely sample, while no appreciable smoothing (FWHM $\approx \sigma_i$) occurs when the intrinsic width is $\gg \sigma_Q$, as observed for the greigite sample. Intermediate cases are plotted in Figure 6 for comparison. A best fit of the central ridge FWHM versus ΔH for the Lake Ely sample is obtained with equation (19) when $\sigma_i < 0.4$ mT, which we take as the upper limit for the intrinsic width (Figure 6). Assuming magnetite composition and $\sigma_i < 0.4$ mT, equation (17) predicts an upper limit of only 9×10^{-4} for the volume concentration of UNISD particles. This concentration corresponds

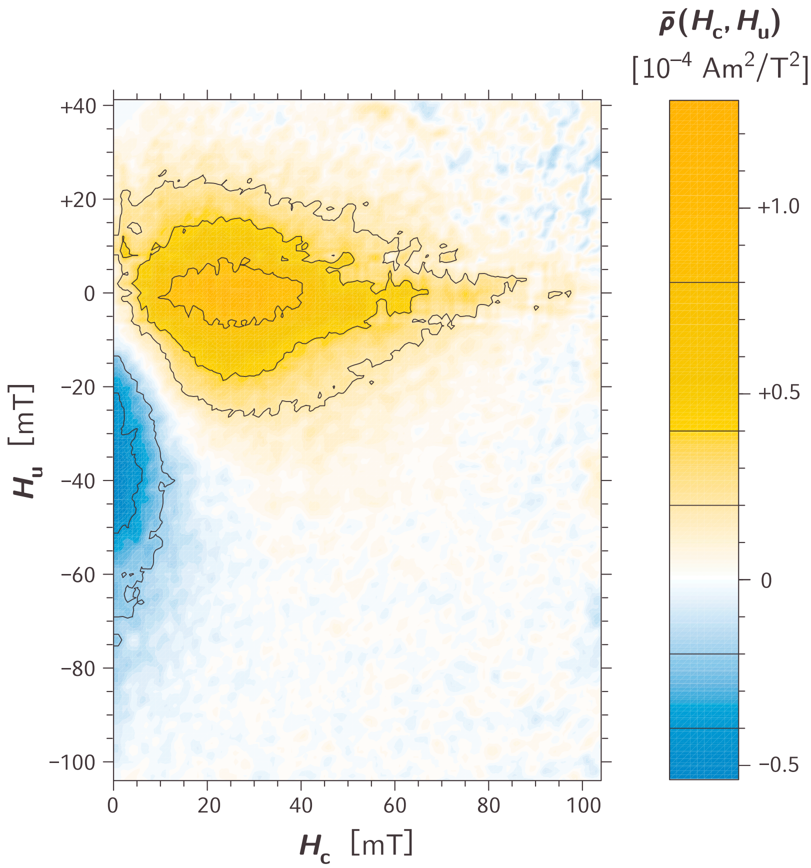

Figure 11. "Ridge-free" FORC function for the Lake Ely sample, obtained by subtracting the central ridge contribution from the FORC diagram of Figure 1, as explained in section 4.6.

to an average distance between particles that is >10 times larger than their size.

4.6. Calculating the Switching Field Distribution From the Central Ridge

[35] The amplitude and width of the central ridge depends on extrinsic parameters such as the measurement resolution, data processing, and particle concentration. More useful characterization of the central ridge is obtained by integrating $\tilde{\rho}_{cr}$ over H_u. The resulting central ridge function

$$\mu_{cr}(H_c) = 2\int_{-\infty}^{+\infty} \tilde{\rho}_{cr}(H_c, H_u)\,dH_u \approx \frac{M_s}{2}\,\overline{S} f(H_c) \qquad (20)$$

depends only on intrinsic properties of the particles. The central ridge function contains all physical information related to ρ_{cr} in simplest form, and is proportional to the switching field distribution. It is the only known parameter that is absolutely not responsive to non-UNISD magnetic components.

[36] The FORC diagram for a mixture of UNISD and non-UNISD particles is the sum of the central ridge $\tilde{\rho}_{cr}$ and the reversible contribution ρ_{ur} of UNISD particles, and a continuous function ρ_{other} representing PSD, MD, or interacting SD particles. These contributions are clearly distinguishable in Figure 1. Separation of $\tilde{\rho}_{cr}$ from other contributions is required to calculate μ_{cr} from equation (20). Measurement resolution therefore becomes critical because the wider the $\tilde{\rho}_{cr}$, the more difficult it is to distinguish it from a continuous background.

[37] Rigorous separation of $\tilde{\rho}_{cr}$ is based on evaluation of the FORC diagram around the H_c axis. Figure 9a is a vertical profile of the FORC function at an arbitrary value of H_c. This profile corresponds to idealized measurements with infinite resolution, where $\rho_{cr}(H_u)$ is a Dirac delta function. The SW model predicts ρ_{ur} to diverge at H_u = 0 [*Newell*, 2005] because of the infinite slope of individual particle hysteresis loops just before switching (Figure 7a). In reality, ρ_{ur} is regularized by thermal activation effects over the entire SD grain

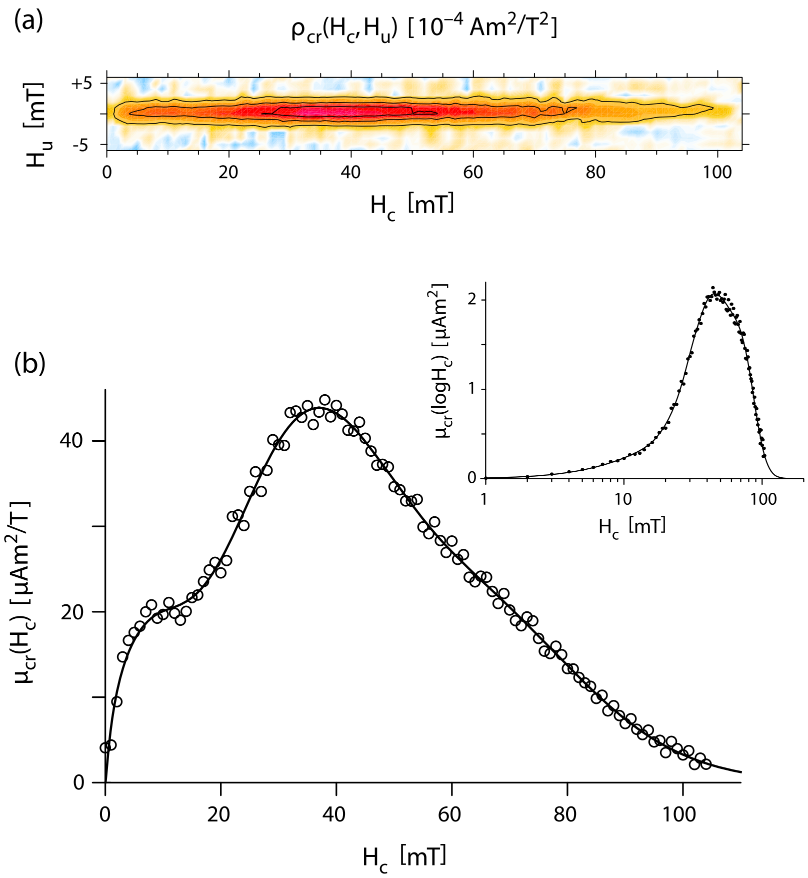

Figure 12. (a) The central ridge, obtained by subtracting the "ridge-free" FORC function of Figure 11 from the FORC diagram of Figure 1. The function is zero outside the range given by $|H_u| \leq 6$ mT. (b) The ridge function, $\mu_{cr}(H_c)$ (open circles), obtained by integrating the central ridge over $|H_u| \leq 6$ mT. The inset shows the same function plotted on a log field scale. Notice how different features of μ_{cr}, such as the two "bumps" on each side of the central maximum, are weighted differently.

size range, so we can safely assume it to be a finite function. FORC data processing, magnetostatic interactions, and thermal activations convert the ideal profile of Figure 9a into that of Figure 9b. FORC data processing has a negligible effect on the continuous background, because of its wide profile. The central ridge is characterized by a finite FWHM given by equation (19), and is significantly >0 only if $|H_u| \leq \eta$ FWHM, where $\eta \approx 1$ depends on the exact shape of the profile. Outside of this region, the FORC diagram is unaffected by the central ridge. Correct separation of the central ridge is possible if the range of H_u values covered by $\tilde{\rho}_{cr}$ is small enough to allow linear extrapolation of $\rho_{ur} + \rho_{other}$ toward $H_u = 0$ without introducing significant errors. This range should not exceed a small fraction of the typical width of $\rho_{ur} + \rho_{other}$ along H_u, and defines the required resolution of the FORC diagram. Measurement points located just outside $|H_u| \leq \eta$ FWHM can be used to extrapolate the "ridge-free" FORC function $\overline{\rho} = \rho_{ur} + \rho_{other}$ near the H_c axis. The central ridge is then obtained by subtracting $\overline{\rho}$ from the FORC diagram. In the Lake Ely example, FWHM $\approx$ 2.4 mT, and points with $|H_u| > 5$ mT (i.e., $\eta \approx 1$) were used to extrapolate $\overline{\rho}$ under the central ridge (Figure 10).

[38] The reconstructed ridge-free FORC function $\overline{\rho} = \rho_{ur} + \rho_{other}$ for the Lake Ely sample is shown in Figure 11. The central ridge, $\tilde{\rho}_{cr} = \rho - \overline{\rho}$, calculated by subtracting $\overline{\rho}$ (Figure 11) from the original FORC diagram (Figure 1), is shown in Figure 12a. Finally, the ridge function was obtained by numerical integration of $\tilde{\rho}_{cr}$ over H_u using equation (20) (Figure 12b). This result is independent of measurement resolution, provided FWHM is sufficiently small for correct isolation of ρ_{cr}. Our procedure for isolating the central

Table 3. Summary of Measured and Inferred Magnetic Contributions to the Remanent Magnetization and to the FORC Function

Contribution	Magnetization (μAm^2)	M_{rs}/M_s	FORC Integral (μAm^2)
UNISD	M_{rs} = 0.447[a]	0.5[b]	$I_{cr} = \int_0^\infty \mu_{cr}(H_c)\mathrm{d}H_c = 0.243$
Other	–	–	$I_{other} \approx 0.286$[c]
Bulk	M_{rs} = 0.508	0.47	$I_{cr} + I_{other} = 0.529$
Saturation	M_s = 1.08	–	–

[a] Calculated from I_{cr} using equation (14) and the SW model ($\overline{S}$ = 0.5438).
[b] By definition of randomly oriented UNISD particles.
[c] $I_{other} = 4\iint_{H_u \geq 0} \overline{\rho}(H_c, H_u)\mathrm{d}H_c\mathrm{d}H_u$, where the factor 4 includes a factor 2 for the variable transformation $(H_c, H_u) \to (H_r, H)$ and another factor 2 for the extrapolation of ρ_{other} below the H_c axis, based on the assumption that ρ_{other} is an even function of H_u.

ridge function is incorporated into the UNIFORC processing code.

5. Discussion

[39] The FORC diagram of the Lake Ely sample contains a central ridge whose intrinsic FWHM is <0.4 mT (Figure 6). We interpret this ridge as the signature of individual SD particles or linear chains of such particles that are extremely well dispersed in the sediment matrix. If these particles are magnetofossils, they must occur in the form of isolated, intact chains. This excludes contributions from magnetotactic bacteria that contain two or more adjacent chains [*Penninga et al.*, 1995; *Hanzlik et al.*, 2002], or magnetosome clusters [*Faivre and Schüler*, 2008], because of the strong magnetostatic interactions expected in such cases. Collapsed chains [*Kobayashi et al.*, 2006] would also not contribute to the central ridge for the same reason. The existence of a central ridge testifies to the integrity of at least some of the magnetofossil chains in the Lake Ely sample. Chain integrity is presumably a prerequisite for preservation of a paleomagnetic signal carried by magnetofossils, and will be compromised by early diagenetic magnetite dissolution [e.g., *Karlin*, 1990; *McNeill*, 1990] and possibly by sediment matrix recrystallization [*McNeill and Kirschvink*, 1993]. The capability of intact chains to survive these processes is poorly known: experiments indicate that ultrasonic disruption of cell membranes does not lead to chain collapse [*Kobayashi et al.*, 2006], and a rock magnetic study on sediments from the Bahamas banks suggests that intact chains must be present in the majority of the sediments [*McNeill and Kirschvink*, 1993]. Magnetic components compatible with nondisrupted magnetofossil chains have also been reported in two pelagic limestones [*Egli*, 2004a]. These interpretations were mainly based on ARM data, while FORC measurements would provide a much more powerful indication for chain integrity.

[40] Three coercivity components can be identified in the central ridge, as suggested by the "bumps" on both sides of the central maximum (Figure 12b). Coercivity analysis of the central ridge will be discussed in detail in another paper (Egli et al., manuscript in preparation, 2010). The low-coercivity component is characterized by a mean switching field of <20 mT, which is small compared to typical values obtained from measurements of whole magnetotactic bacteria cells [*Moskowitz et al.*, 1993; *Kobayashi et al.*, 2006] and magnetofossil components [*Egli*, 2004a]. It is compatible with magnetotactic bacteria grown in the laboratory under unnatural conditions [*Li et al.*, 2009; *Carvallo et al.*, 2009], which are unlikely in nature. Ultrafine magnetite precipitated in aqueous solution, either inorganically [*Maher*, 1988], or by dissimilatory iron reducing bacteria [*Lovley et al.*, 1987], is also compatible with a median switching field of 18–20 mT. The occurrence of such a component in the central ridge would imply that the particles are well dispersed in the sediment matrix, in contrast to laboratory products of dissimilatory iron reduction [*Moskowitz et al.*, 1993], and synthetic clay-magnetite assemblages proposed as analogs to natural aggregates in lake and marine depositional environments [*Galindo-Gonzalez et al.*, 2009].

[41] The saturation remanence of UNISD particles can be estimated from I_{cr} using equation (14) and a hysteresis model for SD particles, which allows one to calculate $\overline{S}$. If we choose SW particles with randomly oriented easy axes (M_{rs} = 0.5 M_s and $\overline{S} \approx 0.5438$), we obtain M_{rs} = 0.447 μAm^2, which is only 12% less than M_{rs} of the bulk sample (Table 3). However, if the UNISD component is dominated by magnetofossil chains, the SW model is not expected to be appropriate and should be replaced by alternative switching models, such

as the chain of spheres fanning [*Jacobs and Bean*, 1955]. The integral of the central ridge-free FORC function (Figure 11) is much larger than the 12% non-UNISD contribution to M_{rs} obtained with the SW model, which suggests that M_{rs} of UNISD particles must be smaller. This implies that $\overline{S} > 0.6$ for magnetofossil components. In a companion paper (Egli et al., manuscript in preparation, 2010) we will estimate $\overline{S}$ on the basis of equation (15) and compare it with models for linear magnetosome chains.

6. Conclusions

[42] We have developed a FORC measurement and data processing protocol for characterizing noninteracting or weakly interacting uniaxial SD particles. Our method is insensitive to admixtures of other magnetic components, and its resolution is limited only by the sensitivity of the instrument used for FORC measurements. The method was tested on a sediment sample from Lake Ely, which is known to contain abundant magnetofossils, where we identified for the first time all FORC signatures predicted for noninteracting SD particles. The FORC diagram of this sample is dominated by a narrow ridge on the H_c axis. This ridge indicates that magnetofossils are extremely well dispersed in the sediment matrix, and that they occur in form of isolated, intact chains. Collapsed or clustered chains, if present, would contribute to other parts of the FORC diagram. Authigenically precipitated ultrafine magnetite or greigite [*Rowan et al.*, 2009] possibly contributes to the low-coercivity component of the central ridge, if well dispersed in the sediment matrix.

[43] We have also demonstrated that the central ridge function, obtained by integration of the central ridge over H_u is proportional to the switching field distribution of the magnetic particles. This allows precise comparison with results obtained from other magnetic characterization techniques. Our Lake Ely example demonstrates the highly discriminative power of FORC measurements, with possible applications ranging from characterization of magnetofossils for paleomagnetic and environmental studies, to detection of highly dispersed SD magnetization carriers in rocks as ideal NRM carriers for paleointensity studies.

Acknowledgments

[44] High-resolution FORC measurements were performed at the Institute for Rock Magnetism, University of Minnesota, which is funded by the National Science Foundation, the Keck Foundation, and the University of Minnesota. A. P. Chen is currently supported by a U.S. Fulbright Fellowship and by the German Research Foundation (DFG project Eg294-1/1). M. Winklhofer is supported by the German Research Foundation (DFG project Wi182814-1). We are indebted to Andrew Roberts, Andrew Newell, and two anonymous reviewers for constructive reviews that significantly improved this paper.

References

Abrajevitch, A., and K. Kodama (2009), Biochemical vs. detrital mechanism of remanence acquisition in marine carbonates: A lesson from the K-T boundary interval, *Earth Planet. Sci. Lett.*, *286*, 269–277, doi:10.1016/j.epsl.2009.06.035.

Bellini, S. (1963), Su di un particolare comportamento di batteri d'acqua dolce, Inst. of Microbiol., Univ. of Pavia, Pavia, Italy. (*Chin. J. Oceanol. Limnol.*, Engl. Transl., *27*, 3–5, 2009.)

Blakemore, R. P. (1975), Magnetotactic bacteria, *Science*, *190*, 377–379, doi:10.1126/science.170679.

Carter-Stiglitz, B., M. Jackson, and B. Moskowitz (2002), Low-temperature remanence in stable single domain magnetite, *Geophys. Res. Lett.*, *29*(7), 1129, doi:10.1029/2001GL014197.

Carvallo, C., A. P. Roberts, R. Leonhardt, C. Laj, C. Kissel, M. Perrin, and P. Camps (2006), Increasing the efficiency of paleointensity analyses by selection of samples using first-order reversal curve diagrams, *J. Geophys. Res.*, *111*, B12103, doi:10.1029/2005JB004126.

Carvallo, C., S. Hickey, D. Faivre, and N. Menguy (2009), Formation of magnetite in *Magnetospirillum gryphiwaldense* studied with FORC diagrams, *Earth Planets Space*, *61*, 143–150.

Chang, S.-B. R., J. F. Stolz, and J. L. Kirschvink (1987), Biogenic magnetite as a primary remanence carrier in limestones, *Phys. Earth Planet. Inter.*, *46*, 289–303, doi:10.1016/0031-9201(87)90191-9.

Chen, A. P., R. Egli, and B. M. Moskowitz (2007), First-order reversal curve (FORC) diagrams of natural and cultured biogenic magnetic particles, *J. Geophys. Res.*, *112*, B08S90, doi:10.1029/2006JB004575.

Cisowski, S. (1981), Interacting vs. non-interacting single domain behavior in natural and synthetic samples, *Phys. Earth Planet. Inter.*, *26*, 56–62, doi:10.1016/0031-9201(81)90097-2.

Dumas, R. K., C.-P. Li, I. V. Roshchin, I. K. Schuller, and K. Liu (2007), Magnetic fingerprints of sub-100 nm Fe dots, *Phys. Rev. B*, *75*, 134405, doi:10.1103/PhysRevB.75.134405.

Egli, R. (2003), Analysis of the field dependence of remanent magnetization curves, *J. Geophys. Res.*, *108*(B2), 2081, doi:10.1029/2002JB002023.

Egli, R. (2004a), Characterization of individual rock magnetic components by analysis of remanence curves, 1. Unmixing natural sediments, *Stud. Geophys. Geod.*, *48*, 391–446, doi:10.1023/B:SGEG.0000020839.45304.6d.

Egli, R. (2004b), Characterization of individual rock magnetic components by analysis of remanence curves, 3. Bacterial magnetite and natural processes in lakes, *Phys. Chem. Earth*, *29*, 869–884.

Egli, R. (2006a), Theoretical aspects of dipolar interactions and their appearance in first-order reversal curves of thermally activated single-domain particles, *J. Geophys. Res.*, *111*, B12S17, doi:10.1029/2006JB004567.

Egli, R. (2006b), Theoretical considerations on the anhysteretic remanent magnetization of interacting particles with uniaxial anisotropy, *J. Geophys. Res.*, *111*, B12S18, doi:10.1029/2006JB004577.

Egli, R., and W. Lowrie (2002), Anhysteretic remanent magnetization of fine magnetic particles, *J. Geophys. Res.*, *107*(B10), 2209, doi:10.1029/2001JB000671.

Faivre, D., and D. Schüler (2008), Magnetotactic bacteria and magnetosomes, *Chem. Rev.*, *108*, 4875–4898, doi:10.1021/cr078258w.

Feinberg, J. M., R. J. Harrison, T. Kasama, R. E. Dunin-Borkowski, G. R. Scott, and P. R. Renne (2006), Effects of internal mineral structures on the magnetic remanence of silicate-hosted titanomagnetite inclusions: An electron holography study, *J. Geophys. Res.*, *111*, B12S15, doi:10.1029/2006JB004498.

Florindo, F., D. B. Karner, F. Marra, P. R. Renne, A. P. Roberts, and R. Weaver (2007), Radioisotopic age constraints for Glacial Terminations IX and VII from aggradational sections of the Tiber River delta in Rome, Italy, *Earth Planet. Sci. Lett.*, *256*, 61–80, doi:10.1016/j.epsl.2007.01.014.

Frankel, R. B., R. P. Blakemore, and R. S. Wolfe (1979), Magnetite in freshwater magnetic bacteria, *Science*, *203*, 1355–1356, doi:10.1126/science.203.4387.1355.

Galindo-Gonzalez, C., J. M. Feinberg, T. Kasama, L. Cervera Gontard, M. Pósfai, I. Kósa, J. D. G. Duran, J. E. Gil, R. J. Harrison, and R. E. Dunin-Borkowski (2009), Magnetic and microscopic characterization of magnetite nanoparticles adhered to clay surfaces, *Am. Mineral.*, *94*, 1120–1129, doi:10.2138/am.2009.3167.

Geiss, C. E., R. Egli, and W. Zanner (2008), Direct estimates of pedogenic magnetite as a tool to reconstruct past climates from buried soils, *J. Geophys. Res.*, *113*, B11102, doi:10.1029/2008JB005669.

Golden, D. C., D. W. Ming, C. S. Schwandt, H. V. Lauer Jr., R. A. Socki, R. V. Morris, G. E. Lofgren, and G. A. McKay (2001), A simple inorganic process for formation of carbonates, magnetite, and sulfides in Martian meteorite ALH84001, *Am. Mineral.*, *86*, 370–375.

Hanzlik, M., M. Winklhofer, and N. Petersen (2002), Pulsed-field-remanence measurements on individual magnetotactic bacteria, *J. Magn. Magn. Mater.*, *248*, 258–267, doi:10.1016/S0304-8853(02)00353-0.

Harrison, R. J., and J. M. Feinberg (2008), FORCinel: An improved algorithm for calculating first-order reversal curve distributions using locally weighted regression smoothing, *Geochem. Geophys. Geosyst.*, *9*, Q05016, doi:10.1029/2008GC001987.

Heslop, D., and A. R. Muxworthy (2005), Aspects of calculating first-order reversal curve distributions, *J. Magn. Magn. Mater.*, *288*, 155–167, doi:10.1016/j.jmmm.2004.09.002.

Hesse, P. P., and J. F. Stolz (1999), Bacterial magnetite and the Quaternary climate record, in *Quaternary Climates, Environments and Magnetism*, edited by B. A. Maher and R. Thompson, pp. 163–198, Cambridge Univ. Press, Cambridge, U. K.

Horng, C.-S., and K.-H. Chen (2006), Complicated magnetic mineral assemblages in marine sediments offshore of southwestern Taiwan: Possible influence of methane flux on the early diagenetic process, *Terr. Atmos. Ocean. Sci.*, *17*, 1009–1026.

Housen, B. A., and B. M. Moskowitz (2006), Depth distribution of magnetofossils in near-surface sediments form the Blake/Bahama Outer Ridge, western North Atlantic Ocean, determined by low-temperature magnetism, *J. Geophys. Res.*, *111*, G01005, doi:10.1029/2005JG000068.

Jacobs, I. S., and C. P. Bean (1955), An approach to elongated fine-particle magnetism, *Phys. Rev.*, *100*, 1060–1067, doi:10.1103/PhysRev.100.1060.

Karlin, R. (1990), Magnetite diagenesis in marine sediments from the Oregon continental margin, *J. Geophys. Res.*, *95*, 4405–4419, doi:10.1029/JB095iB04p04405.

Kim, B. Y., K. P. Kodama, and R. E. Moeller (2005), Bacterial magnetite produced in water column dominates lake sediment mineral magnetism: Lake Ely, USA, *Geophys. J. Int.*, *163*, 26–37, doi:10.1111/j.1365-246X.2005.02735.x.

Kirschvink, J. L. (1982), Paleomagnetic evidence for fossil biogenic magnetite in western Crete, *Earth Planet. Sci. Lett.*, *59*, 388–392, doi:10.1016/0012-821X(82)90140-6.

Kirschvink, J. L., and S.-B. Chang (1984), Ultrafine-grained magnetite in deep-sea sediments: Possible bacterial magnetofossils, *Geology*, *12*, 559–562, doi:10.1130/0091-7613(1984)12<559:UMIDSP>2.0.CO;2.

Kobayashi, A., J. L. Kirschvink, C. Z. Nash, R. E. Kopp, D. A. Sauer, L. E. Bertani, W. F. Voorhout, and T. Taguchi (2006), Experimental observation of magnetosome chain collapse in magnetotactic bacteria: Sedimentological, paleomagnetic, and evolutionary implications, *Earth Planet. Sci. Lett.*, *245*, 538–550, doi:10.1016/j.epsl.2006.03.041.

Kopp, R. E., B. P. Weiss, A. C. Maloof, H. Vali, C. Z. Nash, and J. L. Kirschvink (2006), Chains, clumps, and strings: Magnetofossil taphonomy with ferromagnetic resonance spectroscopy, *Earth Planet. Sci. Lett.*, *247*, 10–25, doi:10.1016/j.epsl.2006.05.001.

Li, J. H., Y. X. Pan, G. J. Chen, Q. S. Liu, L. X. Tian, and W. Lin (2009), Magnetite magnetosome and fragmental chain formation of *Magnetospirillum magneticum* AMB-1: Transmission electron microscopy and magnetic observations, *Geophys. J. Int.*, *177*, 33–42, doi:10.1111/j.1365-246X.2009.04043.x.

Lovley, D. R., J. F. Stolz, G. I. Nord, and E. J. P. Phillips (1987), Anaerobic production of magnetite by a dissimilatory iron reducing microorganism, *Nature*, *330*, 252–254, doi:10.1038/330252a0.

Lowenstam, H. A. (1962), Magnetite in denticle capping in recent chitons (*Polyplacophora*), *Geol. Soc. Am. Bull.*, *73*, 435–438, doi:10.1130/0016-7606(1962)73[435:MIDCIR]2.0.CO;2.

Maher, B. A. (1988), Magnetic properties of some synthetic sub-micron magnetites, *Geophys. J. Int.*, *94*, 83–96, doi:10.1111/j.1365-246X.1988.tb03429.x.

Mayergoyz, I. D. (1986), Mathematical models of hysteresis, *IEEE Trans. Magn.*, *22*, 603–608, doi:10.1109/TMAG.1986.1064347.

McNeill, D. F. (1990), Biogenic magnetite from surface Holocene carbonate sediments, Great Bahama Bank, *J. Geophys. Res.*, *95*, 4363–4371, doi:10.1029/JB095iB04p04363.

McNeill, D. F., and J. L. Kirschvink (1993), Early dolomitization of platform carbonates and the preservation of magnetic polarity, *J. Geophys. Res.*, *98*, 7977–7986, doi:10.1029/93JB00353.

Moskowitz, B. M., R. B. Frankel, and D. A. Bazylinski (1993), Rock magnetic criteria for the detection of biogenic magnetite, *Earth Planet. Sci. Lett.*, *120*, 283–300, doi:10.1016/0012-821X(93)90245-5.

Muxworthy, A. R., and D. J. Dunlop (2002), First-order reversal curve (FORC) diagrams for pseudo-single-domain magnetites at high temperature, *Earth Planet. Sci. Lett.*, *203*, 369–382, doi:10.1016/S0012-821X(02)00880-4.

Muxworthy, A. R., and W. Williams (2005), Magnetostatic interaction fields in first-order reversal curve diagrams, *J. Appl. Phys.*, *97*, 063905, doi:10.1063/1.1861518.

Newell, A. J. (2005), A high-precision model of first-order reversal curves (FORC) functions for single-domain ferromagnets with uniaxial anisotropy, *Geochem. Geophys. Geosyst.*, *6*, Q05010, doi:10.1029/2004GC000877.

Pan, Y., N. Petersen, M. Winklhofer, A. F. Davila, Q. Liu, T. Frederichs, M. Hanzlik, and R. Zhu (2005), Rock magnetic properties of uncultured magnetotactic bacteria, *Earth Planet. Sci. Lett.*, *237*, 311–325, doi:10.1016/j.epsl.2005.06.029.

Passier, H. F., and M. J. Dekkers (2002), Iron oxide formation in the active oxidation front above sapropel S1 in the eastern Mediterranean Sea as derived from low-temperature magnetism, *Geophys. J. Int.*, *150*, 230–240, doi:10.1046/j.1365-246X.2002.01704.x.

Penninga, I., H. de Waard, B. M. Moskowitz, D. A. Bazylinski, and R. B. Frankel (1995), Remanence measurements on individual magnetotactic bacteria, *J. Magn. Magn. Mater.*, *149*, 279–286, doi:10.1016/0304-8853(95)00078-X.

Petersen, N., T. von Dobeneck, and H. Vali (1986), Fossil bacterial magnetite in deep-sea sediments from the South Atlantic Ocean, *Nature*, *320*, 611–615, doi:10.1038/320611a0.

Pike, C. R. (2003), First-order reversal-curve diagrams and reversible magnetization, *Phys. Rev. B*, *68*, 104424, doi:10.1103/PhysRevB.68.104424.

Pike, C. R., and A. Fernandez (1999), An investigation of magnetic reversal in submicron-scale Co dots using first order reversal curve diagrams, *J. Appl. Phys.*, *85*, 6668–6676, doi:10.1063/1.370177.

Pike, C. R., A. P. Roberts, and K. L. Verosub (1999), Characterizing interactions in fine magnetic particle systems using first order reversal curves, *J. Appl. Phys.*, *85*, 6660–6667, doi:10.1063/1.370176.

Pike, C. R., A. P. Roberts, and K. L. Verosub (2001a), First-order reversal curve diagrams and thermal relaxation effects in magnetic particles, *Geophys. J. Int.*, *145*, 721–730, doi:10.1046/j.0956-540x.2001.01419.x.

Pike, C. R., A. P. Roberts, M. J. Dekkers, and K. L. Verosub (2001b), An investigation of multi-domain hysteresis mechanisms using FORC diagrams, *Phys. Earth Planet. Inter.*, *126*, 11–25, doi:10.1016/S0031-9201(01)00241-2.

Preisach, F. (1935), Über die magnetische Nachwirkung, *Z. Phys.*, *94*, 277–302, doi:10.1007/BF01349418.

Roberts, A. P., C. R. Pike, and K. L. Verosub (2000), First-order reversal curve diagrams: A new tool for characterizing the magnetic properties of natural samples, *J. Geophys. Res.*, *105*, 28,461–28,475, doi:10.1029/2000JB900326.

Roberts, A. P., Q. Liu, C. J. Rowan, L. Chang, C. Carvallo, J. Torrent, and C.-S. Horng (2006), Characterization of hematite (α-Fe_2O_3), goethite (α-FeOOH), greigite (Fe_3S_4), and pyrrhotite (Fe_7S_8) using first-order reversal curve diagrams, *J. Geophys. Res.*, *111*, B12S35, doi:10.1029/2006JB004715.

Robertson, D. J., and D. E. France (1994), Discrimination of remanence-carrying minerals in mixtures, using isothermal remanent magnetisation acquisition curves, *Phys. Earth Planet. Inter.*, *82*, 223–234, doi:10.1016/0031-9201(94)90074-4.

Rowan, C. J., and A. P. Roberts (2006), Magnetite dissolution, diachronous greigite formation, and secondary magnetizations in Neogene marine sediments from New Zealand, *Earth Planet. Sci. Lett.*, *241*, 119–137, doi:10.1016/j.epsl.2005.10.017.

Rowan, C. J., A. P. Roberts, and T. Broadbent (2009), Reductive diagenesis, magnetite dissolution, and paleomagnetic smoothing in marine sediments: A new view, *Earth Planet. Sci. Lett.*, *277*, 223–235, doi:10.1016/j.epsl.2008.10.016.

Shcherbakov, V. P., and N. K. Sycheva (1996), Monte Carlo modelling of TRM and CRM acquisition and comparison of their properties in an ensemble of interacting SD grains, *Geophys. Res. Lett.*, *23*, 2827–2830, doi:10.1029/96GL01999.

Shcherbakov, V. P., and N. K. Sycheva (2008), Flocculation mechanism of the acquisition of remanent magnetization by sedimentary rocks, *Izv. Phys. Solid Earth*, *44*, 804–815, doi:10.1134/S106935130810008X.

Shcherbakov, V. P., M. Winklhofer, M. Hanzlik, and N. Petersen (1997), Elastic stability of chains of magnetosomes in magnetotactic bacteria, *Eur. Biophys. J.*, *26*, 319–326, doi:10.1007/s002490050086.

Smirnov, A. V., and J. A. Tarduno (2000), Low temperature magnetic properties of pelagic sediments (Ocean Drilling Program Site 805C): Traces of maghemitization and magnetic mineral reduction, *J. Geophys. Res.*, *105*, 16,457–16,471, doi:10.1029/2000JB900140.

Snowball, I. F. (1994), Bacterial magnetite and the magnetic properties of sediments in a Swedish lake, *Earth Planet. Sci. Lett.*, *126*, 129–142, doi:10.1016/0012-821X(94)90246-1.

Snowball, I. F., L. Zillen, and P. Sandgren (2002), Bacterial magnetite in Swedish varved lake sediments: A potential bio-marker of environmental change, *Quat. Int.*, *88*, 13–19, doi:10.1016/S1040-6182(01)00069-6.

Stoner, E. C., and E. P. Wohlfarth (1948), A mechanism of magnetic hysteresis in heterogeneous alloys, *Philos. Trans. R. Soc. London, Ser. B*, *240*, 599–602.

Tarduno, J. A., R. D. Cottrell, and A. V. Smirnov (2006), The paleomagnetism of single silicate crystals: Recording geomagnetic field strength during mixed polarity intervals, superchrons, and inner core growth, *Rev. Geophys.*, *44*, RG1002, doi:10.1029/2005RG000189.

Vasiliev, I., M. J. Dekkers, W. Krijgsman, C. Franke, C. G. Langereis, and T. A. T. Mullender (2007), Early diagenetic greigite as a recorder of the paleomagnetic signal in Miocene-Pliocene sedimentary rocks of the Carpathian foredeep (Romania), *Geophys. J. Int.*, *171*, 613–629, doi:10.1111/j.1365-246X.2007.03560.x.

Wehland, F., R. Leonhardt, F. Vadeboin, and E. Appel (2005), Magnetic interaction analysis of basaltic samples and pre-selection for absolute paleointensity measurements, *Geophys. J. Int.*, *162*, 315–320, doi:10.1111/j.1365-246X.2005.02429.x.

Weiss, B. P., S. S. Kim, J. L. Kirschvink, R. E. Kopp, M. Sankaran, A. Kobayashi, and A. Komeili (2004), Ferromagnetic resonance and low-temperature magnetic test for biogenic magnetite, *Earth Planet. Sci. Lett.*, *224*, 73–89, doi:10.1016/j.epsl.2004.04.024.

Wilde, H., and H. Girke (1959), Die Messung der Wahrscheinlichkeitsverteilung der Barkhausensprünge in einem Ferromagnetikum, *Z. Angew. Phys.*, *11*, 339–342.

Winklhofer, M., and G. T. Zimanyi (2006), Extracting the intrinsic switching field distribution in perpendicular media: A comparative analysis, *J. Appl. Phys.*, *99*, 08E710.

Winklhofer, M., R. K. Dumas, and K. Liu (2008), Identifying reversible and irreversible magnetization changes in prototype patterned media using first- and second-order reversal curves, *J. Appl. Phys.*, *103*, 07C518.

Yamazaki, T. (2008), Magnetostatic interactions in deep-sea sediments inferred from first-order reversal curve diagrams: Implications for relative paleointensity normalization, *Geochem. Geophys. Geosyst.*, *9*, Q02005, doi:10.1029/2007GC001797.